



NRC Publications Archive Archives des publications du CNRC

Hollow, branched and multifunctional nanoparticles : Synthesis, properties and applications

Ma, Dongling; Kell, Arnold

This publication could be one of several versions: author's original, accepted manuscript or the publisher's version. / La version de cette publication peut être l'une des suivantes : la version prépublication de l'auteur, la version acceptée du manuscrit ou la version de l'éditeur.

For the publisher's version, please access the DOI link below. / Pour consulter la version de l'éditeur, utilisez le lien DOI ci-dessous.

Publisher's version / Version de l'éditeur:

<https://doi.org/10.1142/S0219581X09006419>

International Journal of Nanoscience, 8, 6, pp. 483-514, 2009-07-19

NRC Publications Record / Notice d'Archives des publications de CNRC:

<https://nrc-publications.canada.ca/eng/view/object/?id=89ee6609-c06c-4ca6-9583-25e9b166a203>

<https://publications-cnrc.canada.ca/fra/voir/objet/?id=89ee6609-c06c-4ca6-9583-25e9b166a203>

Access and use of this website and the material on it are subject to the Terms and Conditions set forth at

<https://nrc-publications.canada.ca/eng/copyright>

READ THESE TERMS AND CONDITIONS CAREFULLY BEFORE USING THIS WEBSITE.

L'accès à ce site Web et l'utilisation de son contenu sont assujettis aux conditions présentées dans le site

<https://publications-cnrc.canada.ca/fra/droits>

LISEZ CES CONDITIONS ATTENTIVEMENT AVANT D'UTILISER CE SITE WEB.

Questions? Contact the NRC Publications Archive team at

PublicationsArchive-ArchivesPublications@nrc-cnrc.gc.ca. If you wish to email the authors directly, please see the first page of the publication for their contact information.

Vous avez des questions? Nous pouvons vous aider. Pour communiquer directement avec un auteur, consultez la première page de la revue dans laquelle son article a été publié afin de trouver ses coordonnées. Si vous n'arrivez pas à les repérer, communiquez avec nous à PublicationsArchive-ArchivesPublications@nrc-cnrc.gc.ca.



HOLLOW, BRANCHED AND MULTIFUNCTIONAL NANOPARTICLES: SYNTHESIS, PROPERTIES AND APPLICATIONS

DONGLING MA^{*,†}

*Institut national de la recherche scientifique
University of Quebec, Varennes
Quebec, J3X 1S2, Canada
ma@emt.inrs.ca*

ARNOLD KELL

*Steacie Institute for Molecular Sciences
National Research Council of Canada, Ottawa
Ontario, K1A 0R6, Canada
arnold.kell@nrc-cnrc.gc.ca*

Revised 19 July 2009

Nanoscale materials with various structures have attracted extensive research interest during the past decade. Among them, hollow, branched and multifunctional nanoparticles comprised of two different nanoparticle components are emerging as new classes of interesting nanomaterials owing to the unique optical, catalytic, electrical, magnetic and mechanical properties associated with their unusual morphologies as well as their potential wide range of applications in various fields such as photothermal therapy, diagnosis, drug delivery, catalysis, optoelectronic, electronics and biodiagnostics. In particular, branched nanoparticles promise to serve as building blocks for more complex materials and advanced devices through self-assembly and self-alignment and heterodimeric nanoparticles show promise for the development of tunable magnetic materials and multimodal biodiagnostic imaging tools.

Keywords: Hollow nanoparticles; branched nanostructures; multifunctional nanoparticles.

1. Introduction

For the past two decades, nanomaterials have attracted intensive research interest owing to their unique size-dependent properties, remarkably different from their bulk counterparts.^{1–5} In addition to size, shape and structure details (e.g., surface chemistry and porosity) also strongly influence the physical and chemical properties of nanoscale

materials. As a result, realizing a precise control over the morphology including size, shape and structure details of nanomaterials has been one of the major goals in nanoscience. Great efforts have been devoted towards achieving various nanostructures such as nanocages,^{6–8} nanorods,^{9–11} nanowires,^{12,13} nanodisks,^{14,15} nanocubes,^{16,17} and multipods.^{18–20} These studies are particularly

^{*}Corresponding author.

[†]1650 Boulevard Lionel-Boulet, Varennes, QC J3X 1S2, Canada.

important in understanding the intrinsic structure–property relationship and in uncovering the growth mechanism of specific structures. Beyond of fundamental significance, the elucidation of the structure–property relationship is critical to further design and create novel nanostructures with designed functions and to develop new technologies and applications. Due to diverse optical, chemical, electrical, magnetic and mechanical properties of these nanostructures which often appear quite different from those of normal spherical solid nanoparticles, they are promising candidates for a wide range of applications in various fields of biomedicine,^{21,22} catalysis,^{23,24} optoelectronics,^{25,26} electronics,^{27,28} photonics,^{29,30} and so on.

Among all these novel nanostructures, hollow and branched ones are particularly interesting. Some of them exhibit unusual properties and important applications have been correspondingly envisioned. For example, Au nanocages (nanoparticles with hollow interior and porous walls) with distinct resonance tunability and large absorption cross sections in the near infrared (NIR) are very attractive for the use in the photothermal therapy of cancers.²¹ With large specific surface area, hollow Pd nanoparticles not only reveal high catalytic activity, but also can be used many times without losing their activity, clearly superior to that of solid Pd nanoparticles.³¹ They therefore have high potential to revolutionize the field of catalysis. Semiconducting CdSe tetrapods that can spontaneously orientate with one pod normal to the electrode have demonstrated improved performance in hybrid polymer photovoltaic devices as compared with one-dimensional nanorods due to enhanced charge extraction.³² Branched structures may also serve as promising building blocks for further generation of novel structures with higher complexity and of future electronic, magnetic and photonic devices through self-assembly and self-alignment processes, essential for many practical applications.³³ Hollow nanoparticles such as Au,⁷ Ag,⁸ Pt,⁶ Pd,³¹ ZnO,³⁴ and Cu₂O,³⁵ and branched nanostructures such as CdSe,³⁶ CdS,³⁷ CdTe,¹⁹ Au,³⁸ and Rh¹⁸ have been reported.

In addition to unique nanoparticles constructed from a single material, there is also a significant interest in the development of nanomaterials constructed from at least two different materials. There are a number of strategies capable of merging two different materials into single nanoparticle architectures. Perhaps the most popular approach

involves the encapsulation of a various nanoparticles in a silica or polymer shell. For example, nanoparticles with magnetic nanoparticle and quantum dot components^{39–42} have been prepared through these methods. Conversely, hybrid nanoparticles have also been constructed simply through binding different nanoparticles to the surface of silica or polymer microspheres. This strategy has lead to the development of magnetic nanoparticle/quantum dot,⁴³ magnetic nanoparticle/platinum nanoparticle,⁴³ and magnetic nanoparticle/gold nanoparticle^{43–45} hybrid structures. These hybrid architectures have found utility in both biodiagnostic applications for the magnetic manipulation and detection of DNA,⁴⁵ the magnetic isolation and detection of biomarkers from dilute solution,³⁹ as dual-function probes to both image (magnetic resonance imaging (MRI) contrast enhancement from iron oxide nanoparticles) and destroy cancer cells (Au nanoshell provides photo-thermal heating)⁴³ and in catalytic reactions where the catalyst is magnetically recoverable.⁴³ Though these hybrid structures are robust and useful, there are some fundamentally interesting issues inherent to developing multifunctional nanoparticles where the two different materials are in direct contact with one another rather than simply co-residing in or on a given matrix. Some of the first examples of such hybrid nanostructures were described for quantum dots, where the construction of core@shell were shown to significantly improve the luminescent properties of nanoparticles.^{46–48} In essence, the development of these core@shell quantum dots demonstrates that the combination of these two different materials results in a material that exhibits properties that are completely unique in comparison to each of the individual components alone.

Though the preparation of quantum dots with many different combinations of core@shell structures is quite well known, the development of hybrid structures for metal, metal oxide and quantum dot nanoparticles is only just beginning garner significant interest from the research community. Hybrid nanoparticles comprised exclusively of the two components are thought to be the most effective structures by which dual-function nanoparticles can be constructed, in addition to the promise that combining these materials may uncover some new and interesting properties that have yet to be discovered. A number of protocols have been recently

reported where hybrid nanoparticles comprised of combinations of iron, iron oxide, iron platinum alloy, gold, silver, nickel, nickel oxide, quantum dots and manganese oxide nanoparticles can be readily prepared. The different nanomaterials comprising the hybrid nanoparticles are generally attached through two fundamentally different interfaces. There are heterodimeric and multimeric nanoparticle architectures where the contact between the two materials is limited to a very small interface, and the more common core@shell architecture where intimate interfacial contact between the two materials over the entire surface of the core material is achieved.

In this review, we first outline the wet-chemistry synthesis of hollow and branched nanoparticles as well as their interesting properties and emerging applications in important fields of, e.g., biomedicine and catalysis. Techniques using the physical methods such as vapor–liquid–solid (VLS) and laser ablation to make these nanostructures are not discussed herein. The latter part of this review will focus on the synthetic approaches to construct unique hybrid nanomaterials with either limited contact or core@shell structures, highlight some interesting properties that are inherent to the combination of at least two materials into a single nanoparticle and finally showcase some interesting biological applications that can be carried out with these fascinating materials.

2. Hollow Nanoparticles

Hollow nanoparticles with nonporous or porous walls (i.e., nanocages) have generated much research interest recently because of their tunable structural features, including wall thickness, porosity, interior cavity size and chemical compositions.^{6–8,31,34,35} They have higher surface area and lower density as compared to their filled nanostructures. In addition, their intrinsic properties are expected to be quite different. These unique properties could lead to diverse applications in biomedicine, catalysis and optics.^{21,31} In the following, we discuss their synthesis, properties and potential applications.

2.1. Synthesis

Traditionally, hollow nanostructures are synthesized by coating the surfaces of sacrificial colloidal templates typically polymer or SiO₂ beads with

thin layers of the desired material through layer-by-layer or electroless deposition methods and then selectively removing the templates through calcinations or wet chemical etching. Hollow nanoparticles such as Au,⁴⁹ Pd,³¹ SiO₂,⁵⁰ TiO₂,⁵¹ Au/Pt,⁵² poly-(styrenesulfonate)/poly(allylamine),⁵³ NiO,⁵⁴ α -Fe₂O₃,⁵⁵ ZnO,³⁴ TiO₂,⁵⁶ Gd₂O₃,^{56,57} MoS₂,⁵⁸ MoO₃⁵⁸ and other hollow nanoparticles have been synthesized using this approach. Figure 1 schematically illustrates the formation of hollow Pd nanoparticles and also shows their transmission electron microscopy (TEM) and scanning electron microscopy (SEM) images.³¹ Although this method is straightforward, the nanostructures prepared using this method are often characterized by rough surfaces, nonuniform shell thickness, structural fragility and poor control since they are composed of discrete nanoparticles or ultrafine nanocrystals embedded in disordered areas.³⁴ In addition, the yield is normally low.⁷

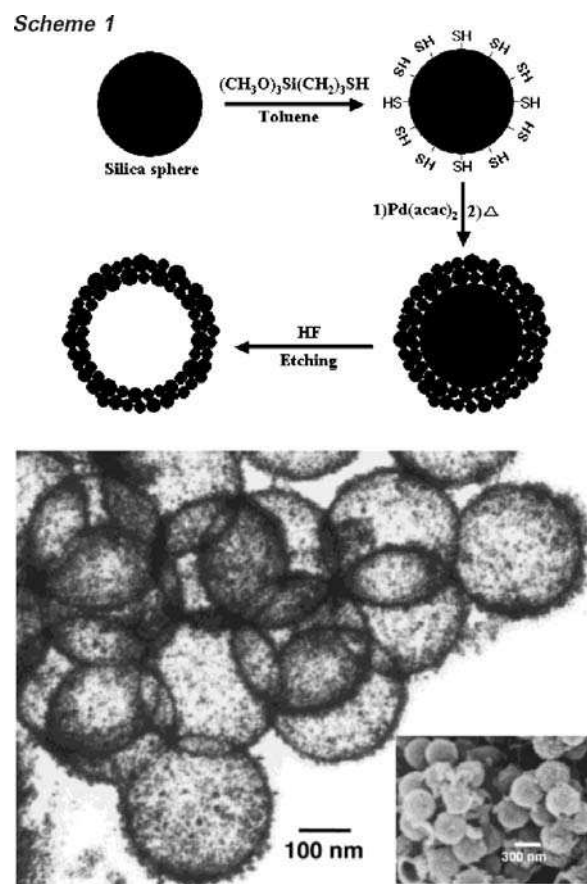


Fig. 1. The procedures used to synthesize Pd hollow spheres and their transmission electron micrograph and scanning electron micrograph (Inset). Reprinted with permission from Ref. 31. Copyright 2002 American Chemical Society.

Galvanic displacement that is based on the differences in the reduction potentials of metals has proved to be a convenient one-step approach capable of fabricating hollow metal nanostructures with well-defined void sizes and homogenous, smooth, highly crystalline walls. Hollow metallic or bimetallic nanostructures composed of less reactive noble metals such as Au, Pt and Pd have been successfully prepared using either Ag or Co as sacrificial colloidal templates in an aqueous medium.^{7,59–62} For example, Xia and co-workers have used Ag templates with a variety of shapes including nanocubes and nanospheres to react with HAuCl_4 in an aqueous medium to generate hollow Ag/Au nanoboxes in a single step.⁷ Figure 2 demonstrates the growth steps in this process. Further reaction of HAuCl_4 with the Au/Ag shell will selectively etch Ag and thus lead to the formation of porous Au nanocages. Interestingly, it is found the morphology of the nanoshell resembles that of the Ag template with its cavity size mainly determined by the dimensions of the template. Using the similar approach, the hollow nanoparticles have also been prepared in an organic phase.^{63,64} The growth details, particularly the evolution process of metals from solid objects into nanocages, however, are found to be different.⁶³ A tighter control over the wall thickness and porosity of Au nanocages has been achieved by using $\text{Fe}(\text{NO}_3)_3$ or NH_4OH , instead of HAuCl_4 , as etchants in the step of transforming seamless Ag/Au alloy nanoboxes to porous Au nanocages.⁶⁵ The operation is based on the concept of decoupling the dealloying of Ag from the Au deposition during this structural transmission. Although in most of the cases, single crystalline walls are obtained through this galvanic displacement approach, the formation of a wall composed of individual nanoparticles has also been reported.⁶

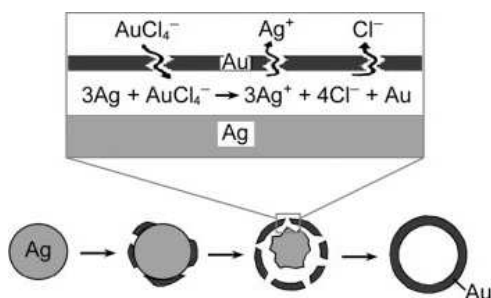


Fig. 2. Schematic illustration of the experimental procedure that generates hollow Au nanoparticles by templating against Ag nanoparticles. Reprinted with permission from Ref. 7. Copyright 2003 Wiley-VCH Verlag GmbH & Co. KGaA.

Kirkendall effect, in which the void is formed due to the considerably large difference in the mutual diffusion rates of two components in a diffusion couple, has also been exploited to prepare hollow nanoparticles. For example, Co nanocrystals have been converted to hollow nanospheres of CoO or cobalt chalcogenides,⁶⁶ CeO_2 nanoparticles to $\text{Ce}_{1-x}\text{Zr}_x\text{O}_2$ nanocages,⁶⁷ Cu_2O nanoparticles to Cu_7S_4 nanocages,⁶⁸ and Ni nanoparticles to Ni_2P hollow nanospheres,⁶⁹ following this mechanism. This approach is especially attractive for synthesizing tiny hollow nanoparticles below 20 nm in diameter.

In addition to the above mentioned “external-templating” approaches, hollow nanostructures have also been demonstrated via a self-templating strategy. For example, Xiong *et al.* have generated single-crystal Pd nanoboxes and nanocages by growing Pd nanocubes first and then oxidatively etching them with O_2 .⁷⁰ Very recently, Wang *et al.* reported a simple self-templating strategy for synthesizing various hollow Ag nanostructures including nanoscale cubic or quasicubic boxes, and triangle and trapeziform rings.⁸ The process involves the modification of the solid Ag nanocrystals by dithiol, and subsequent dissolving of the interior metal and assembly of the outer surface.

A distinctly different approach has been explored by Song *et al.* for the synthesis of highly porous Pt nanocages, which are assembled from joined dendritic Pt nanosheets instead of individual spherical nanoparticles.⁷¹ The nanocages are made by using liposomes containing photocatalyst molecules as a template. The photocatalyst and light induce the nucleation and growth of Pt nanoparticles, which then act as efficient catalysts for their own growth into dendritic nanosheets and interconnected network.

Other different yet related approaches have also been employed to synthesize hollow nanoparticles such as hydrothermal,^{72,73} emulsion,^{74,75} and micelle⁷⁶ methods.

2.2. Optical and catalytic properties

Hollow nanoparticles offer advantages of high surface area and low density as well as show intriguing optical properties and catalytic activities different from their filled counterparts.^{6,7,31,58,70,77} Herein, we outline the surface plasmonic and catalytic behavior of hollow nanoparticles.

2.2.1. Optical properties

The surface plasmon resonance (SPR) was theoretically explained by Mie in 1908⁷⁸ and the Mie's theory, which considers the wavelength-dependent scattering and absorption cross-sections of solid spherical particles, agrees well with experimental spectra in the size regime >20 nm until the normal incidence absorption no longer shows a plasmon resonance for bulk metals. According to the theoretical prediction and also validated experimentally, Au solid nanospheres would normally have an extinction peak in the visible range, approximately in between 510 and 650 nm depending on their sizes.⁷⁷ The formation of hollow nanospheres and nanocages allows achieving tunable SPR in the NIR.

Figure 3(a) compares the ultraviolet-visible-near-infrared (UV-Vis-NIR) extinction spectra of Au solid nanoparticles (~ 50 nm in diameter) and hollow nanospheres (~ 50 nm in core diameter and ~ 4.5 nm in wall thickness).⁷ The solid nanospheres display an intense and sharp peak at ~ 530 nm, while the SPR peak for hollow nanospheres is broader and red-shifts to ~ 680 nm. This result is consistent with the Mie calculation when it is assumed that the interior of hollow nanospheres is completely filled with water, which is the dispersion medium in this study. According to the Mie theory, the SPR band will shift to red if a solid core is replaced by a material having a refractive index higher than 1.0 (water: 1.33). Figure 3(b) plots the SPR peak shift ($\Delta\lambda_{\max}$, relative to the peak recorded with water as the surrounding medium) with respect to the refractive index (n) of the dispersion medium. The results show that the hollow Au nanospheres are about seven times more sensitive (by calculating $\Delta\lambda_{\max}/\Delta n$) to the change of environments.

The SPR can be extended even further into the NIR by synthesizing nanocages. Figure 4 shows how the SPR band changes as the 75-nm Ag nanocubes are reacting with different volumes of 1 mM HAuCl_4 solution.⁶¹ As more HAuCl_4 solution is added, the SPR peak is continuously red-shifted from ~ 425 to ~ 750 nm (Fig. 4(a)). The disappearance of the characteristic Ag SPR at ~ 425 nm with the addition of 0.6 ml of HAuCl_4 solution indicates the structural transition from pure Ag templates to homogeneous Au/Ag nanoshells. The further gradual shifts to 750 nm have been attributed to slightly increasing void sizes. As shown in below, for the

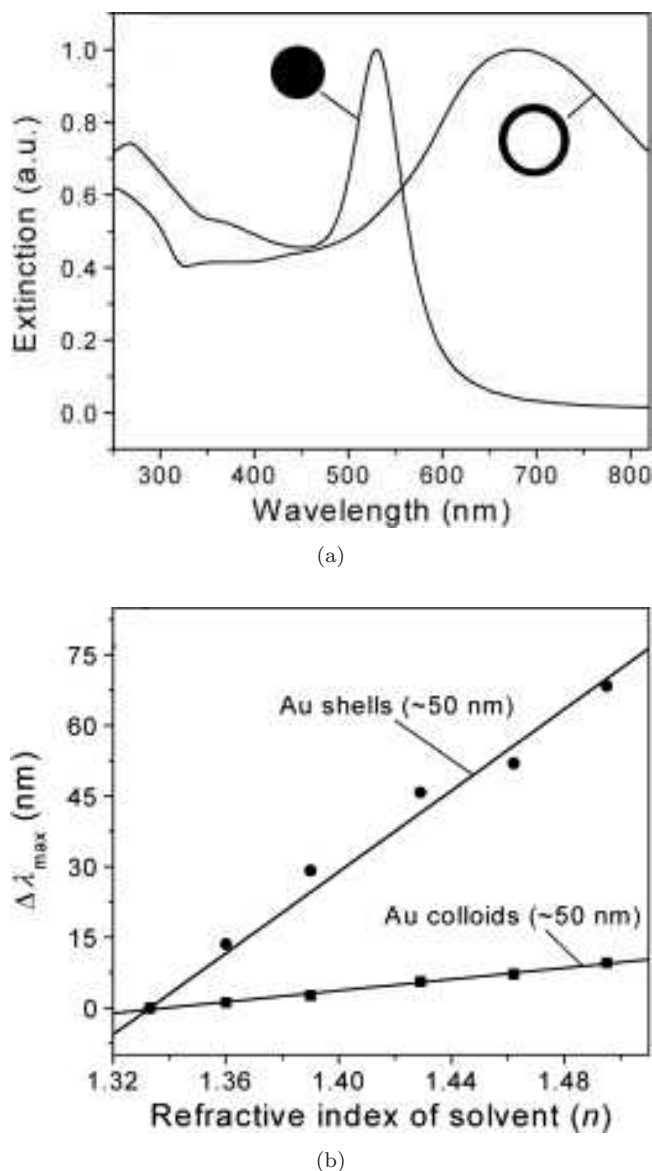


Fig. 3. (a) A comparison between the UV-Vis extinction spectra of Au solid colloids ~ 50 nm in diameter and Au hollow nanoparticles with core diameter of ~ 50 nm and wall thickness ~ 4.5 nm. (b) Plot of the dependence of peak shift ($\Delta\lambda_{\max}$, relative to the peak position obtained with water as dispersion solvent) on the refractive index (n) of surrounding medium. The sensitivity factors $\Delta\lambda_{\max}/\Delta n$, are ~ 60 and ~ 410 nm/RIU for solid and hollow nanoparticles, respectively. Reprinted with permission from Ref. 7. Copyright 2003 Wiley-VCH Verlag GmbH & Co. KGaA.

similar thickness, larger the void size is, the longer wavelength the SPR band (with an increasingly larger contribution from scattering) is situated. Even higher volumes lead to dealloying and selective dissolution of Ag. This causes the formation of pinholes with increasingly larger dimensions in the Au/Ag walls (and thus the formation of nanocages), responsible for further spectra red-shift from ~ 750

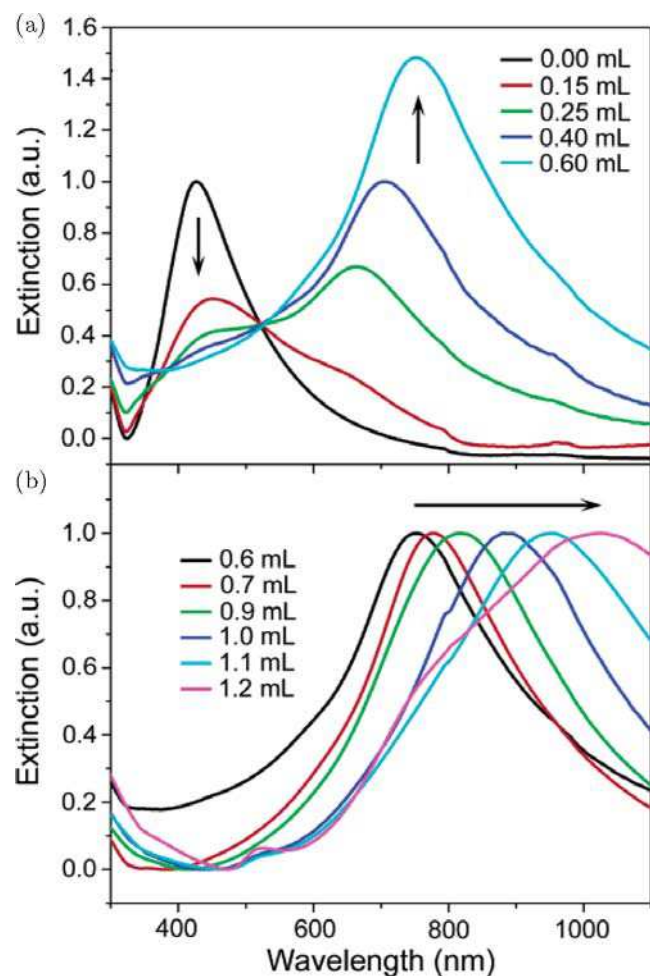


Fig. 4. UV-Vis-NIR extinction spectra of an aqueous dispersion of silver nanoparticles before and after reacting with different volumes (as indicated on each panel) of 1 mM HAuCl_4 aqueous solution: (a) the formation of complete Au/Ag nanoshells through galvanic replacement reaction between Ag templates and HAuCl_4 solution and alloying between Au and Ag and (b) the formation of porous Au nanocages through dealloying and selective dissolution of Ag. Reprinted in part with permission from Ref. 61. Copyright 2003 American Chemical Society.

to ~ 1030 nm (Fig. 4(b)). The SPR peak position is found sensitive to the relative ratio of wall thickness to the diameter of the cavity. The SPR peak of Au nanocages derived from 100-nm Ag nanocubes can be tuned to 1200 nm,⁷⁷ whereas the Au nanocages derived from 11-nm Ag nanocrystals exhibit an SPR peak only at 616 nm.⁶³ Figure 5 shows the discrete dipole approximation (DDA) results for two Au nanocages with different inner edge lengths (30 versus 50 nm) with same wall thickness (~ 5 nm).⁷⁷ It can be seen that although with the similar wall thickness, the larger nanocage shows the SPR peak

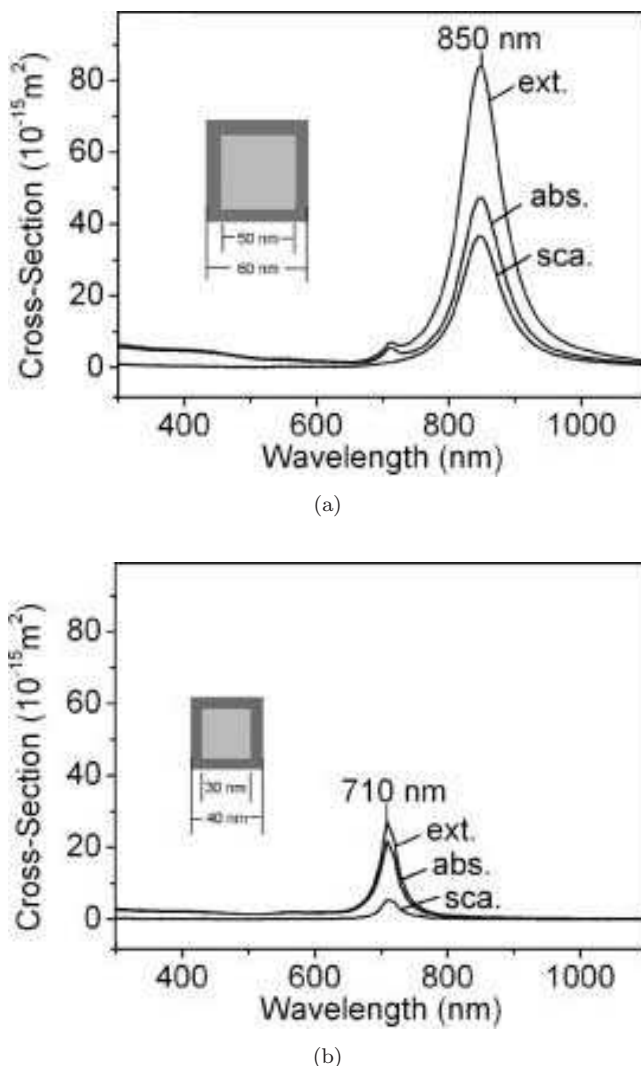


Fig. 5. Extinction spectra calculated using the DDA method for Au nanocages having same wall thickness of 5 nm, while different inner edge lengths: (a) 50 nm and (b) 30 nm. Reprinted with permission from Ref. 77. Copyright 2005 Wiley-VCH Verlag GmbH & Co. KGaA.

at a longer wavelength (850 versus 710 nm). In addition, the contribution from absorption and scattering to the extinction is quite different for these two nanocages: absorption dominates for the 30 nm nanocage; whereas, scattering becomes similarly important as absorption for the 60 nm nanocage. Although the porosity of the nanocages has little effect on the SPR peak position, the magnitude of both the scattering and absorption increases as the porosity of the nanocages increases. Moreover, it is worth mentioning that Au nanocages have the calculated absorption cross-section at least five orders of magnitude larger than organic chromophores.⁷⁷

Solid metal particles that normally do not exhibit any resonance in the visible region could exhibit an SPR band by processing them into hollow ones. For instance, Xiong *et al.* found that the SPR band of Pd nanoparticles can be tuned from 410 to 520 nm by emptying their interiors.⁷⁰

It can be seen that not only the SPR band can be tuned through controlling structural parameters of hollow nanostructures, the magnitude of both scattering and absorption cross-sections can also be adjusted. This tunability is highly desirable as it enables tailor-making nanomaterials for a variety of applications.

2.2.2. Catalytic properties

Porous hollow nanospheres or nanocages have demonstrated significantly higher catalytic activity as compared to their solid counterparts, which has been largely attributed to their high specific surface area, resulting in more unsaturated surface coordination sites for molecule adsorption and reactions.^{6,31,58,73,74,79,80} Pores present on the shell allow efficient mass-transfer of species into the cavity and thus their access to both the inner and outer surface of the hollow nanoparticles. Liang and co-workers reported that the catalytic activity of Pt hollow nanospheres in the room temperature oxidation of methanol is twice that of the solid Pt nanoparticles (Fig. 6) and they attributed this enhanced catalytic activity to the larger surface area in hollow nanospheres.⁶ Yang *et al.* demonstrated similarly improved catalytic behavior of Pt hollow nanoparticles. By normalizing the current densities in the voltammograms by the accessible surface area in hollow and solid nanoparticles, they found that the two voltammograms collapse into a common one, suggesting that the higher catalytic activity of the hollow nanospheres is purely a surface area effect.⁸⁰

The higher catalytic activity is also likely arising from increased surface defects according to Dhas and Suslick.⁵⁸ They found hollow MoS₂ nanospheres exhibit substantially superior catalytic activity in the hydrodesulfurization (HDS) of thiophene as compared to solid nanoparticles and commercial micronized MoS₂ powders. Since only Mo atoms situated at the edges of the MoS₂ layer are responsible for catalyzing the reaction, the authors believe the superior HDS activity of the

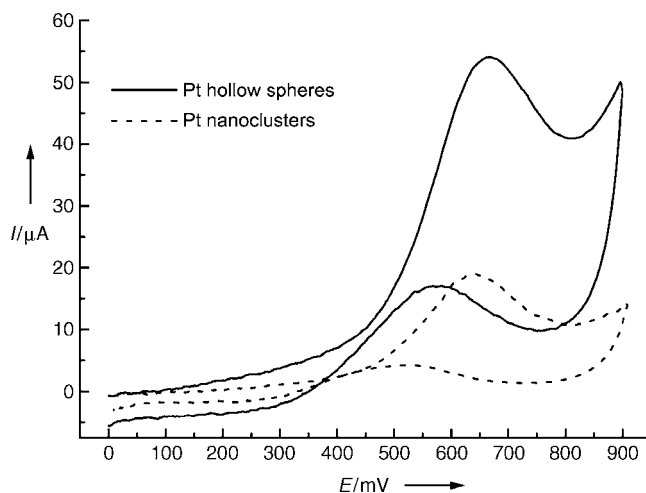


Fig. 6. Cyclic voltammograms of Pt solid nanoclusters (dashed line) and hollow nanospheres (solid line) on a glass carbon disk electrode in H₂SO₄ (0.5 M) and methanol (0.6 M). The same loading of nanospheres and solid nanoclusters was applied to the electrodes (0.0175 mg cm⁻²). Scan rate = 50 mVs⁻¹. Reprinted with permission from Ref. 6. Copyright 2004 Wiley-VCH Verlag GmbH & Co. KGaA.

hollow MoS₂ is in part due to the high density of edge defects observed in hollow nanoparticles. This deduction is supported by their observation that reducing the number of defect sites through high-temperature annealing could lead to the decrease in catalytic activity of the hollow nanospheres. Chen *et al.* have also attributed the enhanced catalytic activity for oxygen reduction of porous Pt nanospheres to both large surface area and high density of defects at the shell surface.⁷⁹

An interesting result was reported by Chen *et al.*⁷⁴ They found that K_xMnO₂ hollow nanospheres demonstrate much higher catalytic activity for oxidative decomposition of formaldehyde than honeycomb nanospheres although the surface area of the latter is nearly two times as high as that of the former. The authors believe it is mainly because that the hollow K_xMnO₂ nanospheres could adsorb and retain formaldehyde for a longer period of time than the honeycomb K_xMnO₂ nanospheres and eventually enhance the oxidation of formaldehyde.

In addition to excellent catalytic activity, hollow nanoparticles also show considerably improved stability. Hyeon *et al.* reported that hollow Pd nanospheres can be reused in Suzuki cross coupling reactions many times without loss of catalytic activity, which is in clear contrast to solid Pd nanoparticles that usually lose their catalytic activity after one round.³¹

2.3. Applications

Despite recent advances in synthesizing hollow nanospheres or nanocages with controlled morphologies and in investigating their unique properties, and relatively high expectation of their usefulness in a variety of applications, there is only limited number of articles reporting on their potential applications. Herein, we outline the application of hollow nanospheres and nanocages in the biomedical sector and catalysis.

2.3.1. Biomedicine

With unique optical properties, high specific surface area, and interior cavity, hollow nanospheres and nanocages have large potential to be used in bioimaging, photothermal therapy and drug delivery.

MRI is a noninvasive, high-resolution, three-dimensional imaging technique and has been widely used in clinical practice. Contrast agents are often required to improve the contrast between normal and diseased tissues and to map biological functions. Hollow Gd_2O_3 nanospheres have been found to be capable of providing high-contrast magnetic resonance (MR) images based on *in vitro* MR assays.⁵⁶ As compared with a commercially available Gd-diethylenetriamine penta-acetic acid, the hollow nanospheres have a nearly two times high relaxivity r_1 (17.7 versus $9.2 \text{ S}^{-1}\text{mM}^{-1}$). The largely brightened T_1 -weighted images have been attributed to the large surface area of hollow nanospheres, which favors proton coordination and the interaction between water and Gd^{3+} ions. Au_3Cu_1 hollow nanospheres also show promising MR contrast effect, in both *in vitro* and *in vivo* studies.²² Pre- and post-contrast T_1 - and T_2 -weighted images in mice are shown in Fig. 7. It is clear that hollow nanospheres considerably enhance signal intensity in the cardiac area in T_1 -weighted images. More interestingly, the hollow nanospheres also brightly lit the blood vessels of the liver in T_2 -weighted images. These *in vivo* experiments indicate that the hollow nanospheres not only have potential as positive-contrast agents, but also are quite effective for use in MR angiography as blood-pool agents.

Optical coherence tomography (OCT), which can noninvasively image the differences between the normal and diseased tissues has appeared as a promising diagnostic tool. Au nanocages

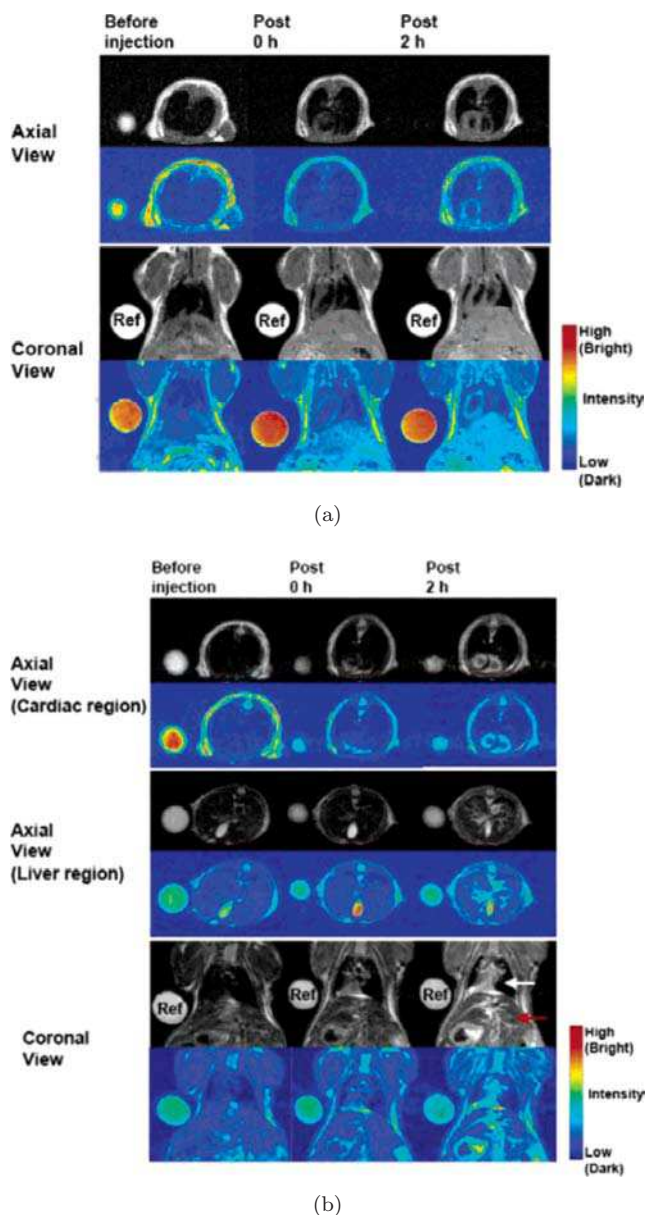


Fig. 7. *In vivo* progressive MRI events and color maps. (a) T_1 -weighted and (b) T_2 -weighted images of male BALB/c mice at the indicated temporal points (pre-injection, immediately post-injection, and 2 h post-injection) in this experiment with Au_3Cu_1 nanocapsules. The arrows in (b) indicate the increase in signal intensity and show visualized vessels for the thorax and liver regions in T_2 -weighted images (coronal view). Reprinted with permission from Ref. 22. Copyright 2007 American Chemical Society.

with moderate scattering cross-section of $\sim 8.10 \times 10^{-16} \text{ m}^2$ but a very large absorption cross-section of $\sim 7.26 \times 10^{-15} \text{ m}^2$ have been demonstrated to be able to largely attenuate light and thus enhance the contrast of OCT images of phantom samples.⁸¹

Photoacoustic tomography (PAT) is a novel imaging technique combining the merits of optical

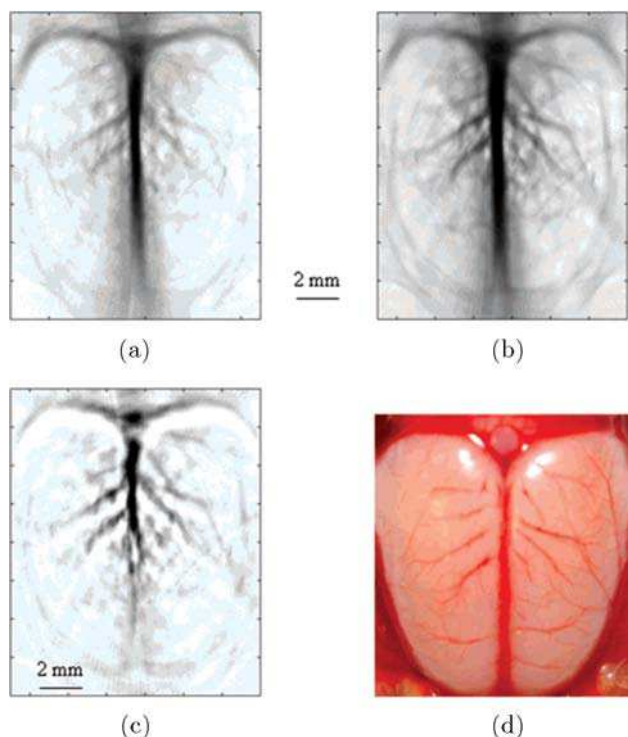


Fig. 8. Noninvasive PAT imaging of a rat's cerebral cortex (a) before the injection of nanocages and (b) about 2 h after the final injection of nanocages, which is the peak enhancement point. (c) A pixelwise differential image (image B-image A). (d) An openskull photograph of the rat's cerebral cortex. Three successive injections were administered in these results. Reprinted with permission from Ref. 82. Copyright 2007 American Chemical Society.

and ultrasound imaging. The feasibility of Au nanocages as an intravascular contrast agent for PAT of small animals has been demonstrated recently.⁸² Figure 8 shows the PAT images of the cerebral cortex of a rat before and after the injection of nanocages. Figure 8(b) reveals the brain vasculature with greater clarity than Fig. 8(a) due to the injection of Au nanocages, which greatly enhances the contrast between blood in vessels and the background brain tissues because of their large optical absorption.

Hollow nanospheres can also serve as hosts of labeling materials and thus increasing the fluorescence density in conventional fluorescence imaging techniques. Due to the larger surface area, hollow nanospheres can bind and load more molecules than solid counterparts. For example, propidium iodide, a standard fluorophore used in staining dead cells and thus in distinguishing between live and dead cells, have been loaded to solid and hollow Au nanospheres.⁸³ A five-fold increase in the mean

fluorescence intensity has been found for the cells stained with Au nanocages.

Hollow nanospheres with large surface area and empty core space can encapsulate large quantity of drug molecules and serve as drug carriers.^{76,84–86} For example, hollow biocompatible and biodegradable calcium phosphate nanospheres have been demonstrated to be able to load amylase molecules and release them in a precisely controlled way by ultrasonic treatments.⁸⁴ More interestingly, hollow nanospheres may cross the blood brain barriers and deliver drugs to the brain.⁸⁶ Figure 9 exhibits the concentration of doxorubicin (DOX), an anticancer agent, in the brain of mice at different time intervals after the injection of hollow polymer nanoparticles loaded with DOX. DOX can be detected even after 24 h, in contrast to free DOX solution which cannot be detected even at the initial time after injection. This exciting performance may be due to the enhanced interaction between polymer spheres and brain microvessel endothelial cells.

Photothermal therapies have emerged as a minimally invasive technique for selectively killing cancer cells with little injury to the intervening and surrounding normal tissues as compared to conventional surgical treatments, radiotherapy, and chemotherapy of tumors. Large absorption cross sections and remarkable resonance tunability of Au nanocages make them promising photothermal agents for cancer treatments. Au nanocages that are tuned to strongly absorb in the NIR, a region where optical absorption in tissue is

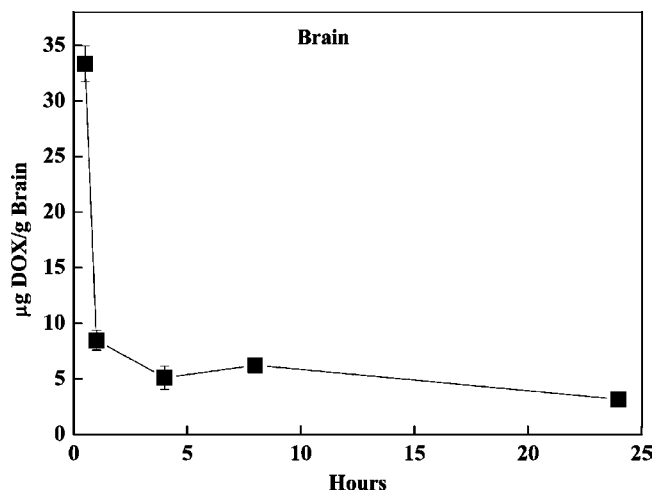


Fig. 9. The DOX concentration in brain at different times after injecting DOX-loaded chitosan-poly(acrylic acid) nanospheres. Reprinted with permission from Ref. 86. Copyright 2007 American Chemical Society.

minimal and penetration is optimal, are particularly attractive for this application. Immuno gold nanocages (~ 45 nm in edge length) have been shown to cause the selective, thermal destruction of cancer cells with an intensity threshold of 1.5 W/cm^2 ,²¹ substantially lower than those reported for gold nanoshells (35 W/cm^2)⁸⁷ and gold nanorods (10 W/cm^2).⁸⁸ In control experiments, cells not treated by immuno gold nanocages exhibit no observable loss of viability. The amount of cellular death can be controlled by both the exposure time and power density of the laser.⁸⁹

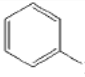
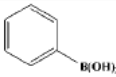
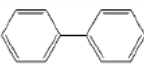
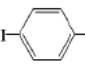
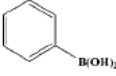
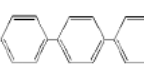
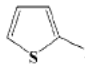
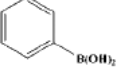
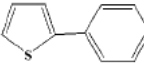
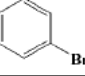
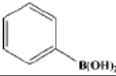
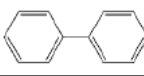
2.3.2. Catalysis

Highly effective and stable yet economical catalysts are required in various practical applications. Porous hollow nanospheres or nanocages exhibiting superior catalytic activity and re-usability as well as with remarkable characteristics of low density and cost-effectiveness are particularly attractive for applications in catalysis. In addition, due to the surface porosity and the presence of the interior cavity, hollow nanoparticles also serve as hosts for immobilizing active catalytic nanoparticles to increase their structural stability during reactions. Several types of reactions including cross-couplings, oxidations and hydrogenations have been conducted using hollow nanosphere or nanocage based catalysts.^{6,31,34,58,73,74,79,80,90–93}

Suzuki reaction couples arylboronic acids and aryl halides to form biaryls, which Pd nanoparticles have been most commonly used to catalyze. Table 1 summarizes the yield of Suzuki reactions of various aryl iodides (or arylbromides) and phenylboronic acid when hollow Pd spheres are used as a catalyst.³¹ It can be seen that the hollow Pd spheres are highly efficient catalysts when aryl iodides are used as reactant, whereas five times more Pd catalysts are required to achieve a similar yield when arylbromides are used.

Oxidation reactions of organics are very important in many industrial processes and are particularly important for removing pollutants or hazardous wastes from air and water. The oxidative decomposition of formaldehyde to CO_2 , a major indoor air pollutant, has been conducted at relatively low temperatures by using highly active hollow K_xMnO_2 nanospheres.⁷⁴ The conversion of formaldehyde reaches 61.8% at 60°C and 100% at 80°C . Pt and Co–Pt hollow nanoparticles have been used as catalysts for methanol oxidation and

Table 1. Suzuki cross-coupling reaction for various substrates.^a Reprinted with permission from Ref. 31. Copyright 2002 American Chemical Society.

Entry	Aryl halide	Boronic acid ^b	Time (h)	Product	Yield (%) ^c
1			3		99
2			24		96
3			3		97
4 ^d			24		90

^aReaction conditions: 10 mg of hollow Pd spheres (3 mol%), 3 mmol aryl iodide, 6 mmol phenylboronic acid, 12 mmol K_3PO_4 , 50 mL of EtOH under reflux.

^b12 mmol of phenylboronic acid was used for diiodobenzene.

^cIsolated yield.

^d50-mg hollow Pd sphere (15 mmol%) was used for bromobenzene.

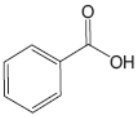
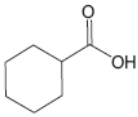
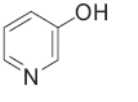
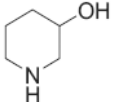
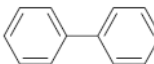
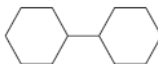
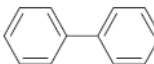
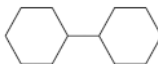
demonstrated greatly enhanced activity, important for the anode electrocatalysis of the direct methanol fuel cells.^{80,90} As another example, photocatalytic degradation of organics has been carried out using NiO, Fe_2O_3 , Pt–ZnO and Au–ZnO hollow nanoparticles.^{34,54,73}

Hydrogenation reactions are one of the most common reactions catalyzed by transition metal nanoparticles. Pt or Rh nanoparticles incorporated in hollow carbon nanospheres have recently been used to catalyze the hydrogenation of 1-hexene, 2-hexene, cyclohexene, benzoic acid, 3-hydroxypyridine and 3-hydroxypiperidine. In all cases, the catalytic activity of hollow nanoparticle based catalysts is significantly higher than that of conventional catalysts. Table 2 summarizes the catalytic activity of Rh-hollow carbon for hydrogenation of various aromatic and heterocyclic compounds at 353 K under 0.5 MPa of H_2 .⁹¹ It can be seen that the novel hollow-structured catalyst is highly active.

3. Branched Nanostructures

A great deal of efforts has been directed toward the synthesis of branched nanostructures including tripods, tetrapods and multipods.^{18–20,36–38,94–109} They are compelling because of anticipated unique

Table 2. Hydrogenation of aromatic and heterocyclic compounds catalyzed by Rh nanoparticles loaded in hollow carbon spheres.^a Reprinted with permission from Ref. 91. Copyright 2008 Wiley-VCH Verlag GmbH & Co. KGaA.

Entry	Substrate	Product	Rh [μmol]	Time [h]	Conversion [%]	Yield [%]
1			0.23	6	89	85
2			0.23	6	98	98
3			0.46	6	92	59 ^[b]
4			0.46	14	99	97

^aConditions: 0.25 mmol substrate, 5 cm³ water, 0.5 MPa H₂, 353 K.

^bPhenylcyclo-hexane (partially hydrogenated intermediate product) was obtained with 33% yield.

optical, electrical, magnetic and mechanical properties associated with their unusual structures as well as their emerging applications in stronger composites, in “bottom-up” self-assembly toward advanced materials and future devices, and in more effective photovoltaics.^{32,33} So far, the reports on the properties and applications of branched nanocrystals still remain very limited. In the following, we will describe the wet-chemistry synthesis of branched nanostructures and also briefly outline their properties and applications.

3.1. Synthesis

Growth of highly anisotropic shapes is a highly kinetic-driven process and typically proceeds through two mechanisms, i.e., seeded growth and oriented attachment.^{18–20,95} The branched nanostructures synthesized through wet chemical approaches were first reported in a series of semiconducting materials such as CdS,³⁷ CdSe,¹⁰⁵ and CdTe,¹⁹ and they are all grown through seeded growth. A common feature of these semiconductor materials is that they possess polytypism, i.e., the presence of two or more crystal structures of similar energy. For example, in CdSe, the (111) of the cubic zinc blende has a perfect lattice match with the (0001) of the wurtzite hexagonal phase. Therefore, by manipulating the surface energy at nanoscale, it allows the generation of a well-defined,

uniform tetrapod structure via the controlled nucleation of a pyramidal seed of zinc blende followed by the epitaxial growth of four arms at the tetrahedral angle which have the wurtzite structure of the inherently anisotropic nature along the *c*-axis. The arm growth is thus exclusively along the [1000] direction of the hexagonal phase. Reaction temperature, ligands and monomer concentrations are all found to be influential factors in shape control. Lower temperature normally favors the formation of branched structures in a kinetic region, while higher temperature spherical shapes dominated by thermodynamic growth. Both phosphonic acids and amines have been used to synthesize anisotropic branched nanocrystals.^{19,37,105} According to Peng *et al.*, however, the monomer concentration is the real determining factor for the anisotropic crystal growth because the multiple growth centers at the end of each branch must be fed with a very high diffusion flux to keep all branches in the 1D-growth mode.^{104,105} Figure 10 illustrates the effect of monomer concentrations on the shape of nanocrystals.¹⁰⁴ The formation of the unique magic sized nuclei is thought to be a result of the extremely high chemical potential environment, that is, very high monomer concentrations in the solution. Both the width and length of four arms can be independently controlled in this seeded growth process. Branched structures of single phase semiconducting materials have also been produced. Lee *et al.* reported that PbS tetrapods with four pods at a separation angle of 90°C which corresponds to their rock salt structure can be grown from the four opposite faces of the (100) faces of the truncated octahedral seeds at a reduced temperature.¹⁰²

Branched semiconductor nanocrystals have also been synthesized using “heterogeneous” seeds. Kuno and co-workers have employed a

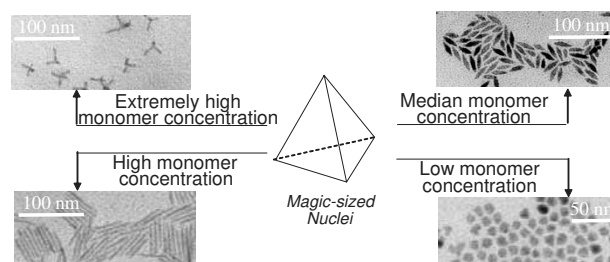


Fig. 10. Monomer-concentration-dependent growth paths of CdSe nanocrystals. Reprinted with permission from Ref. 104. Copyright 2003 Wiley-VCH Verlag GmbH & Co. KGaA.

solution-liquid-solid (SLS) approach, analogous to the traditional VLS method, by designing low-melting Au/Bi catalyst nanoparticles, for the synthesis of CdSe, CdTe and PbSe branched nanostructures including tripod, v-shape, y-shape, “merge-y” and T-shape structures.^{96,99,101} In the tripods of CdSe and CdTe the core has a zinc blende phase and the arms zinc blende/wurtzite phase admixture.^{96,101} In contrast to v-shape, y-shape, and tripod morphologies observed in CdSe and CdTe due to their underlying zinc blende and wurtzite lattices, mainly the right-angle and T-shape structures are observed in PbSe intrinsically determined by its rock salt structure.⁹⁹ In all cases, a geminate nucleation mechanism is responsible for the branching with metal/chalcogen stoichiometry playing the most important role in dictating branching. Multiple nanowires form and orient on the surface of a given liquid Au/Bi nanoparticle when sufficient precursors are present in the system to achieve not only supersaturation, but also the growth of more than one arm.

Branched metal nanoparticles have been recently reported for Au,^{38,97,103} Pt,^{98,106,109} and Rh.¹¹⁰ They are typically prepared through the kinetic control in conjunction with selective adhesion of molecules to particular crystal facets which leads to the difference in the growth rate of different facets and thus the preferential growth along a particular crystallographic direction. Unlike semiconductor nanocrystals such as CdSe for which the intrinsic polytypism has been exploited to produce branched two-phase structures, branched metal nanostructures only consist of a single phase. Single crystalline Rh multipods have been produced from a homogeneous seeded growth, where small Rh nanocrystals stabilized with poly(vinylpyrrolidone) (PVP) serve as seeds, at a reduced temperature by Hoefelmeyer *et al.*; higher temperatures lead to the formation of cubes.¹¹⁰ Humphrey *et al.* have also demonstrated that the rate of rhodium monomer addition is critical for the shape control, regardless of thermodynamic factors.¹⁸ Rapid addition yields single crystalline multipods (tripods, tetrapods) with a yield as high as ~90%, while slow monomer addition forms block-shaped particles. The tripod and tetrapod Au nanocrystals without stacking faults or twins have been synthesized via a simple chemical reduction in an aqueous system at room temperature by Chen *et al.*³⁸ Cetyltrimethylammonium bromide (CTAB) is found to be necessary for obtaining such

structures, while Ag seeds apparently increase the yields of branched nanocrystals. Teng *et al.* illustrated that high-population of well-defined Pt tetrapods, resembling those observed for II–VI quantum dots of CdSe, can be prepared in an organic phase by using a trace amount of Ag.¹⁰⁶ The presence of Ag effectively triggers the nucleation and growth of Pt nanoparticles at temperatures below that for the homogeneous reaction and favoring the kinetically controlled anisotropic growth of Pt in the presence of surfactants. Bipods and tripods have also been formed in this process. The introduction of inorganic species could also provide a powerful means for controlling the shape of metallic nanoparticles. Herricks *et al.* found that by varying the ratio of NaNO₃ to H₂PtCl₆ (the precursor of Pt), the morphology of Pt nanoparticles can evolve from irregular spheroids to octapods and tetrapods.⁹⁸ It may be because that the nitrite reduced from nitrate by PtCl₄²⁻ could form stable complexes with both Pt(II) and Pt(IV) species and hence, greatly slow down the reduction of Pt precursors. As such, the growth rates associated with different crystallographic directions are altered, which ultimately leads to the formation of different morphologies.

Oriented attachment is another mechanism responsible for the anisotropic growth. It occurs by attachment of high surface energy facets of seeds, and hence eliminating high-energy facets and conserving more stable ones. Although this process, typically manipulated by surfactants, often leads to the formation of rods and wires, complex shapes have also arisen from it.^{95,111,112} For example, Cheng *et al.* highlighted the synthesis of single crystalline PbMoO₄ dendrites by a simple hydrothermal method in the presence of surfactants and confirmed that the dendritic structure is achieved through oriented attachment of nanoparticles along crystallographically specific direction by using TEM to monitor the evolution of the structures (Fig. 11). Tripods and tetrapods are transitive species in this process.⁹⁵

Hyperbranched structures without specific growth directions of arms are reported by Lou *et al.* (Fig. 12).¹⁰³ They have prepared hyperbranched Ag nanostructures in an aqueous solution containing trisodium citrate and L-ascorbic acid at room temperature by tuning reaction parameters. The arms grow in any radial direction and the growth is kinetically controlled. These hyperbranched structures are only present as the metastable intermediate

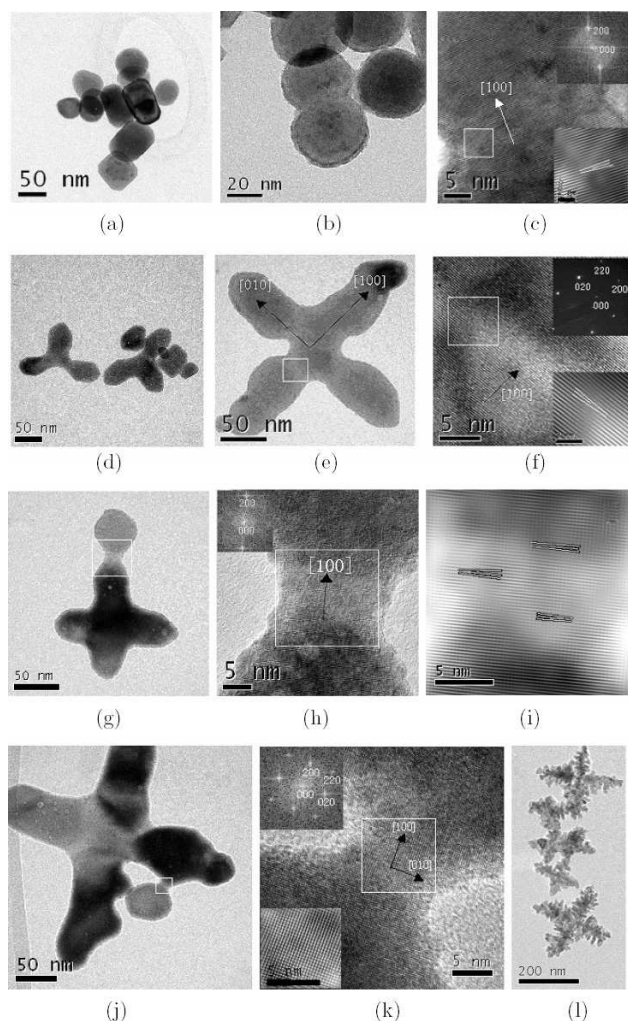


Fig. 11. TEM and high-resolution TEM (HRTEM) images and selected area electron diffraction (SAED) patterns of PbMoO_4 crystals obtained at the different stages of hydrothermal reaction: (a) the initial particles before attachment; (b) a pair of the typical attached particles; (c) HRTEM image of the connecting region of the attached particles in Fig. 3(B), the upper inset is the Fourier transform and the lower inset the reconstructed lattice image from the specified square area; (d) the typical three-armed particles; (e) a typical four-armed particle; (f) HRTEM image of the connecting region of the attached particles in Fig. 3(E), the upper inset is the SAED pattern of the four-armed particle and the lower inset the reconstructed lattice image from the specified square area; (g) TEM image showing attachment of a new particle to elongate the arm; (h) HRTEM image of the bottleneck region in Fig. 3(G) and the corresponding Fourier transform (upper inset); (i) reconstructed image from the square area in Fig. 3(H); (j) TEM image of attachment of a new particle to the lateral of an arm forming the branch; (k) HRTEM image of the bonding region in Fig. 3(J), the upper inset is the Fourier transform and the lower inset the reconstructed image from the square region; (l) TEM image of scabbled dendrites. Reprinted with permission from Ref. 95. Copyright 2005 American Chemical Society.

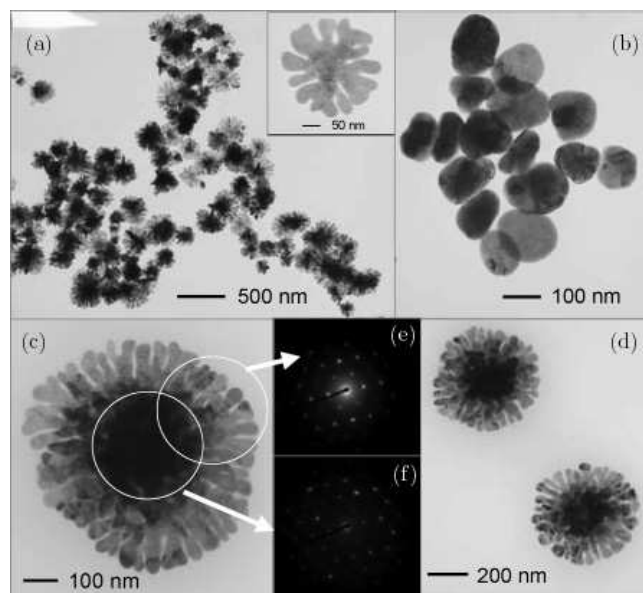


Fig. 12. TEM images of silver nanocrystals (0.1 mL of trisodium citrate, 0.3 mL of L-ascorbic acid, 30 min of seeding, and 30 min of reaction (a), where the inset shows a high-magnification 2D structure; (b) nanoparticles corresponding to (a) with a few days of reaction; (c) same conditions with (a) but without seeding, where (e) and (f) are the corresponding electron diffraction patterns for the selected area in (c); and (d) same conditions with (c) but with 0.6 mL of L-ascorbic acid. Reprinted with permission from Ref. 103. Copyright 2006 American Chemical Society.

species toward final quasi-spherical or disk-like nanoparticles.

3.2. Properties

Branched nanoparticles with tunable arm length and width, interconnected structures and large surface area are expected to have properties different from their spherical counterparts. In the following, we outline their optical, electrical and magnetic properties.

Branched noble metal nanoparticles exhibit a shape-dependent plasmon resonance. Figure 13 shows the variation of the UV-Vis-NIR spectra of Ag nanoparticles as their shape evolve from hyperbranched (as shown in Fig. 12) to quasi-spherical or disk-like nanoparticles with reaction time.¹⁰³ All the spectra show two peaks: one located at 330–380 nm that may be attributed to the out-of-plane quadrupole and the other at 1160–1170 nm that may arise from the in-plane dipole resonance of edges longer than 100 nm or the strong coupling of anisotropic arms. The hyperbranched silver nanoparticles also exhibit a

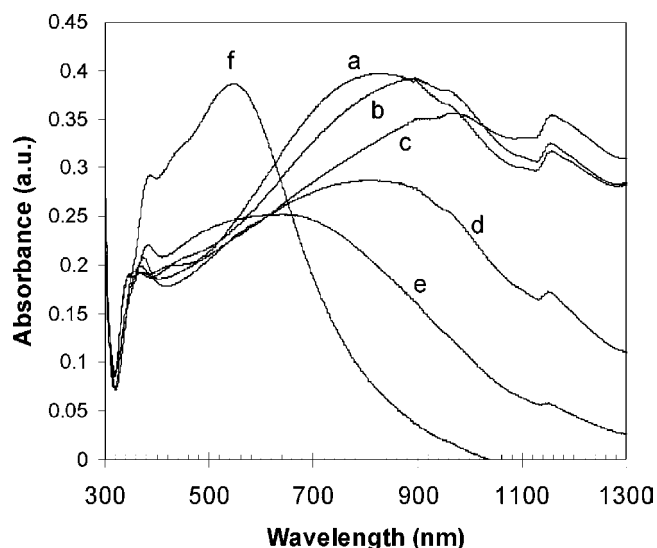


Fig. 13. UV-Vis-NIR spectra of silver nanostructures corresponding to the same conditions as those in Fig. 12 at different times: (a) 2 min; (b) 10 min; (c) 1 h; (d) 6 h; (e) 22 h; and (f) 2 days. Reprinted with permission from Ref. 103. Copyright 2006 American Chemical Society.

broad peak around 800–940 nm, which may be attributed to in-plane dipole plasmon resonance and shift following the shape evolution. Eventually, this peak disappears and a strong and narrow peak arises at ~ 450 – 550 nm, corresponding to final quasi-spherical or disk-like nanoparticles. Hao *et al.* studied the optical properties of branched Au nanoparticles and found the similar red-shift of the plasmonic band in branched nanoparticles as opposed to spherical ones (650–700 nm versus 500–530 nm).⁹⁷ The branched Au nanoparticles with smaller average sizes show plasmonic peaks at shorter wavelengths. From DDA calculations, they found the surface plasmon resonance of the branched Au nanoparticles is mainly determined by in-plane dipole excitation associated with the sharp tips and is most sensitive to the length and the sharpness of the tips. Figure 14 shows the schematic representation of a symmetrical three-tipped Au nanoparticle that is used in the DDA calculations and the calculated E-field external to a three-tipped Au nanoparticle upon excitation at the plasmon maximum.⁹⁷ It is clear that the calculated maximum field enhancement occur at the sharp tips, useful for achieving large surface enhanced Raman scattering.

Manna *et al.* investigated the optical properties of semiconducting tetrapods.¹⁹ It can be seen in Fig. 15, that CdTe tetrapods having comparable

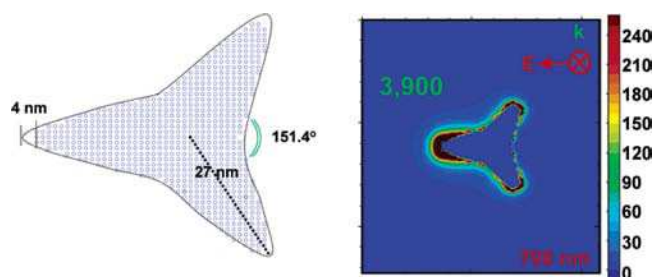


Fig. 14. (Left) Schematic representation of a symmetrical three-tipped Au nanocrystal that is used in the DDA calculations, showing the outline of the particle before snapping, and the DDA grid after snapping. (Right) E-field enhancement contours external to a symmetrical three-tipped gold nanocrystal for polarization along one tip and with the wavelength taken to be the plasmon peak at 700 nm. The peak value of $|E|^2$ at the particle tip is 3900 times the applied field. Reprinted with permission from Ref. 97. Copyright 2004 American Chemical Society.

arm lengths but different diameters show remarkable differences in their absorption peak position (Fig. 15, left), whereas spectra of tetrapods with comparable diameters but different arm lengths are almost identical (Fig. 15, right), suggesting the band gap is determined by the diameter of the hexagonal arms.

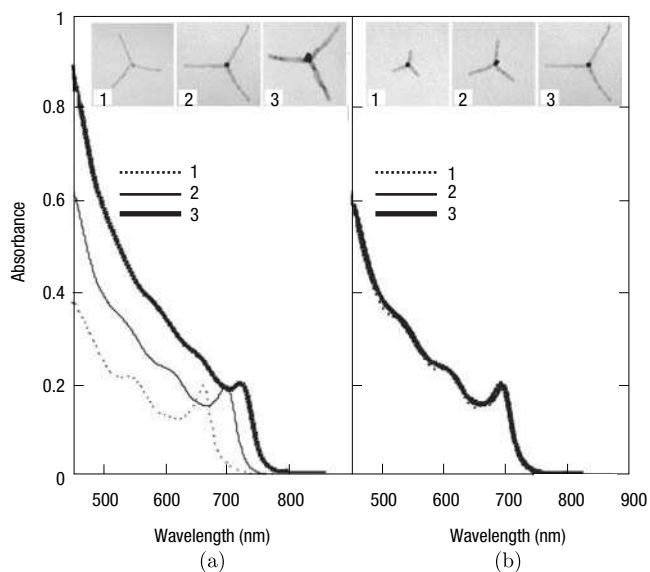


Fig. 15. Influence of the shape of CdTe tetrapods on optical absorption spectra. Ensemble optical absorption spectra a, for a series of tetrapods having comparable arm lengths but different diameters, and b, for a series of tetrapods having comparable arm diameters but different lengths. The confinement energy is mainly dictated by the arm diameter. From Ref. 19. Reprinted by permission from Macmillan Publishers Ltd: Nature Mater. (Ref. 19), Copyright (2003).

Electrical behavior of an individual ZnO tetrapod has also been studied by depositing W and Pt electrodes at the three ends of pods to form Ohmic and Schottky contacts, respectively.¹¹³ Dark current–voltage measurements show rectifying behavior and with increasing excitation power densities, the device converts from a rectifying to an Ohmic behavior. This performance has been attributed to a flattening of the energy bands due to the migration of photogenerated carriers within the space charge region at the metal–semiconductor interface.

Due to the presence of large surface area, interesting magnetic behavior have been observed very recently in branched Pt nanoparticles by Zhang *et al.*¹⁰⁹ As shown in Fig. 16, at room temperature, amine-coated spherical Pt nanoparticles have a very low magnetization (1×10^{-3} emu/g) as expected for paramagnetic materials. In clear contrast, the branched Pt nanoparticles are ferromagnetic and possess a much higher magnetization (10×10^{-3} emu/g) and a coercivity of 106 Oe at room temperature. Although the exact mechanism of this anomalous ferromagnetism in branched noble metal nanoparticles needs to be further investigated and elaborated, it was deduced that the permanent magnetic moment may be introduced by the locally enhanced density of states at the broken symmetry around the surface and charge transfer between surface Pt atoms and surfactant molecules and the huge specific surface area in

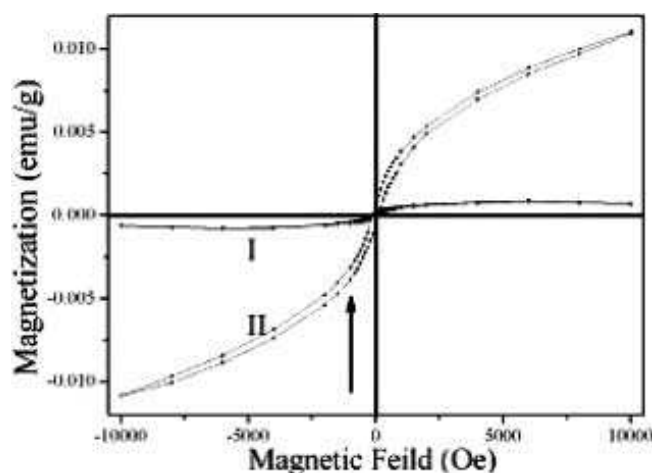


Fig. 16. Magnetization (M) versus magnetic field (H) loops for spherical nanoparticles (I) and branched nanoparticles (II) at 300 K. From Ref. 109. Reprinted in part with permission from Ref. 109. Copyright 2008 American Chemical Society.

branched nanoparticles greatly enhances this surface magnetic moment effect.

3.3. Applications

Branched structures such as tetrapods are expected to be important alternatives to conventional fillers such as fibers and rods for enhancing mechanical properties of polymers.¹⁹ In addition, branched structures may serve as building blocks for more complex materials and advanced devices through self-assembly and self-alignment.^{33,95,112} Figure 17 demonstrates this concept by showing structures that have been formed or anticipated from branched nanoparticles.^{33,112}

Semiconducting tetrapods with the inherent property of self-aligning on a substrate with one arm always towards one electrode has been exploited to improve the efficiency of bulk-heterojunction quantum dot-polymer solar cells.^{32,114} Sun *et al.* highlighted that the photovoltaic devices fabricated from blends of branched CdSe nanoparticles and a conjugated polymer

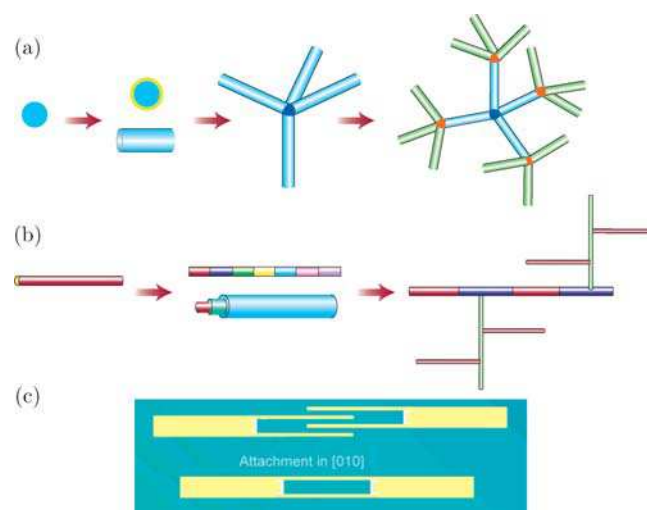


Fig. 17. Emerging diversity in nanocrystal and nanowire building blocks. (a) Progression of nanocrystal structures from homogenous clusters, to core@shell and elongated structures, to branched tetrapod and multi-branched materials. (b) Progression of nanowire structures from uniform wires, to structures modulated in the axial and radial directions, and finally to multi-branched materials. In both sequences, distinct colors are shown to indicate variations in material composition and/or doping. (c) Self assembly of two fork-like nanostructures into a new type of complex nanostructures and a rectangular hole structure. (a, b): Reprinted by permission from Macmillan Publishers Ltd: Nature Mater. (Ref. 33), copyright (2003). (c) Reprinted with permission from Ref. 112. Copyright 2003 American Chemical Society.

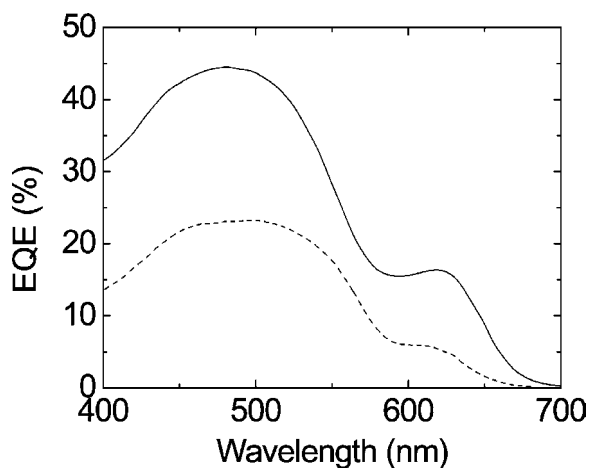


Fig. 18. Short-circuit external quantum efficiency (EQE) action spectra of photovoltaic devices containing CdSe nanorods (---) and tetrapods (—). Reprinted with permission from Ref. 32. Copyright 2003 American Chemical Society.

give improved performance compared with devices made from nanorod-polymer blends (as shown in Fig. 18) due to the fact that 3D CdSe tetrapods have improved electron transport perpendicular to the plane of the device and thus improved electron extraction as compared to 1D nanorods.³² Zhou *et al.* studied the nanocrystal composition of tetrapods on the photovoltaic performance of quantum dot-polymer hybrid solar cells and found with increasing Se content in the $\text{CdSe}_x\text{Te}_{1-x}$ nanocrystals ($x = 0, 0.23, 0.53, 0.78, 1$), the open circuit voltage, short-circuit current and power conversion efficiency of the devices all increase. This effect has been explained by the difference of the band level between the tetrapods and the polymer.¹¹⁴

Optically pumped lasing has been demonstrated in ZnO tetrapods¹¹⁵ and the wurtzite facets at the end of each leg are suggested to act as sufficiently high-quality UV optical mirrors. Newton *et al.* compared the photoluminescence spectra of a cluster of randomly oriented tetrapods and a single tetrapod that has one arm aligned parallel with the incident laser beam and found quite a different response.¹¹⁶ Although both show a UV peak at 3.2 eV arising from interband transitions and a visible peak at 2.3 eV from surface defects, the individual tetrapod shows the significantly increased UV peak. The enhancement is attributed to the fact that the vertical leg of the tetrapod acts as a Fabry-Perot resonant cavity for photons of this energy.

4. Multifunctional Nanoparticles

4.1. Nanoparticle heterodimers and multimers

There has been a tremendous amount of excitement centered on the development of heterostructured hybrid nanoparticles comprised of at least two components. Some of the most interesting nanoparticle architectures are heterodimers or multimers of nanoparticles comprised of two distinct material components held together by nanometer size contacts. These structures are fascinating because they are stable despite the fact that there can be quite large lattice mismatches between the crystalline phases of the two nanoparticle components. Some of the most sought after heterostructure architectures incorporate both magnetic and signaling components into a single nanoparticle. Examples of the types of signaling components that have been incorporated into these hybrid architectures include gold,^{117,119–122} silver,^{118,123,124} and quantum dots.^{125,126} The following sections will highlight some of the interesting synthetic protocols that lead to the development of these unique architectures, the properties inherent to the hybrid nanoparticles and the biodiagnostic applications that can be carried out with the resulting nanomaterials.

4.1.1. Synthesis

Hybrid nanoparticles with noble metal or quantum dot and magnetic components are generally synthesized through the seeded growth of one nanoparticle upon the surface of the other.^{117–124} Where gold (or silver) metal nanoparticle-magnetic nanoparticle conjugates are prepared, Au (or Ag) nanoparticles support the growth of the magnetic components. For example, Au nanoparticles stabilized by long-chain organic ligands are mixed with precursors capable of generating iron oxide or ferrite-based nanoparticles. Upon refluxing in high boiling solvents, the magnetic nanoparticle precursors follow reaction pathways analogous to that for the preparation of homogeneous magnetic nanoparticles,¹²⁷ but in the presence of the Au nanoparticle seeds the growth of the magnetic nanoparticle occurs preferentially on the surface of the existing nanoparticles and there is very little homogeneous nucleation to generate nonhybrid nanoparticles.^{118–122,124} There is very strong evidence from TEM analysis that the growth of Fe_3O_4 nanoparticles on the surface of the Au nanoparticles is epitaxial.^{119,120,122} Figure 19 shows that the (111)

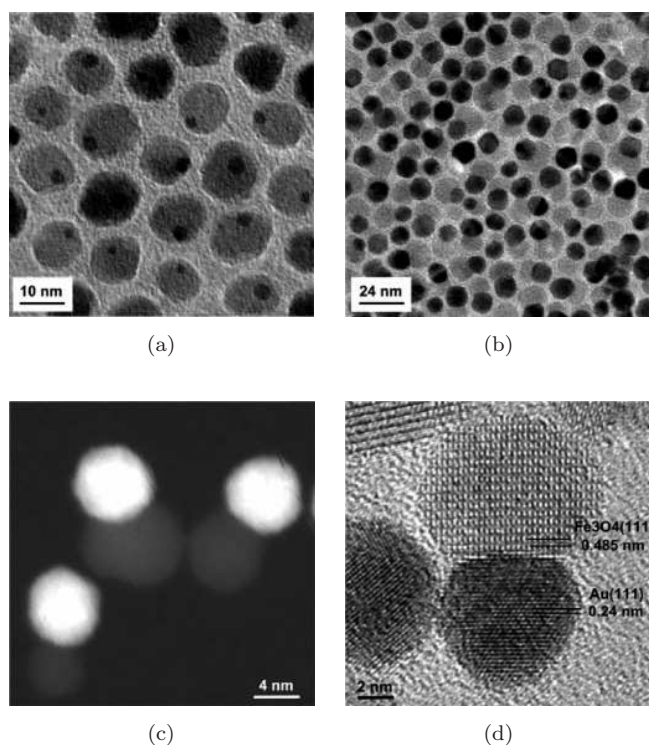


Fig. 19. TEM and scanning transmission electron microscopy (STEM) images of the dimeric Au-Fe₃O₄ nanoparticles: (a) TEM image of the 3–14 nm Au-Fe₃O₄ particles; (b) TEM image of the 8–14 nm Au-Fe₃O₄ particles; (c) high angle annular dark field scanning transmission electron microscopy (HAADF-STEM) image of the 8–9 nm Au-Fe₃O₄ particles; and (d) HRTEM image of one 8–12 nm Au-Fe₃O₄ particle. Reprinted with permission from Ref. 122. Copyright 2005 American Chemical Society.

lattice planes in the cubic Fe₃O₄ domains are parallel to the (111) face centered cubic lattice planes of Au.¹²² The relative sizes of the Au and Fe₃O₄ nanoparticles could be tuned simply by changing the Fe₃O₄ precursor: Au nanoparticle ratio. Yu and Shi independently reported that seeding the growth of more than one Fe₃O₄ nanoparticle from the Au nanoparticles only occurs when solvents with aromatic groups (benzyl and phenyl ether) are utilized. The possible reasons for this are highlighted in Sec. 4.1.2.1. where the properties of the hybrid nanoparticles are discussed. In contrast, Wei *et al.* found that changing the polarity of the solvent system utilized for the nanoparticle synthesis did not affect the architecture of the hybrid nanoparticles.¹²⁰ Wei was, however, able to exert impressive control over the number of Fe₃O₄ nanoparticles that could be grown on the surface of the Au nanoparticle simply by changing the Fe₃O₄ precursor: Au nanoparticle ratio.¹²⁰ By changing this ratio Wei demonstrated that the nanoparticle architecture can

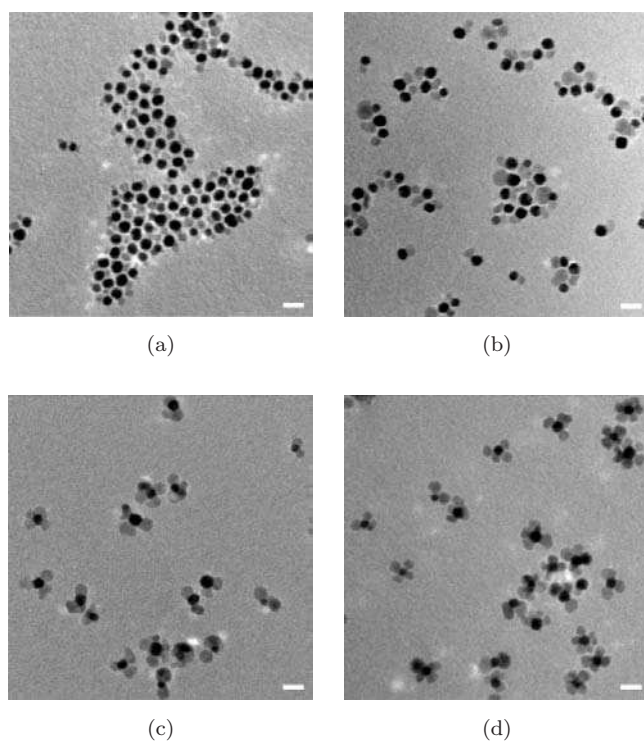


Fig. 20. TEM images of Au-Fe₃O₄ composite nanoparticles prepared with different ratios of Au-Fe₃O₄ precursors. Note that the Fe₃O₄-Au ratio increases from a–d, where it is smallest in (a) and largest in (d). The dark portions of Au/Fe₃O₄ particles correspond to gold while lighter ones to iron oxide. All scale bars are 20 nm. Reprinted with permission from Ref. 120. Copyright 2008 Wiley-VCH Verlag GmbH & Co. KGaA.

be tuned from dimeric structures similar to that described by Yu.¹²² to nanoflower architectures with gold nanoparticles anchoring 2–4 Fe₃O₄ “petals” (Fig. 20). Though the exact reasoning for the dimeric versus multimeric architectures is not completely clear (in fact, Wei and Yu utilized the same Fe₃O₄ precursors and got different results), there is certainly consensus agreement that the Fe₃O₄ are grown from facet regions on the Au nanoparticles, and each different facet should be capable of supporting an Fe₃O₄ nanoparticle if the synthetic conditions can be tuned to allow it.^{119,120,122}

Shi was able to utilize a similar strategy to prepare Au-PbS nanoparticles from Au nanoparticles and Pb and S precursors.¹¹⁹ Because sulfur has a strong affinity for both Pb and Au, the authors could take advantage of the inherent competition between Au and Pb²⁺ to interact with sulfur in order to tune the morphology of the resulting nanoparticles.¹¹⁹ For example, by keeping the Pb:S ratio constant and only changing the gold

nanoparticle concentration, the morphology could be tuned from a dimeric architecture to a multi-meric geometry where two or more PbS nanoparticles could be linked to the surface of the gold nanoparticle. Again, there is strong evidence that the PbS nanoparticles grow epitaxially from the surface of gold nanoparticles under these high temperature conditions. The synthetic principles outlined by Yu and Shi are highly reproducible and have been exploited by several other groups to develop hybrid nanoparticles for a variety of applications that will be highlighted in a later section.^{118,121,124} In addition, Choi and co-workers were able to use a similar strategy to produce hybrid nanoparticles with an enormous amount of variety, including Pt-, Ni- and Au-Fe₃O₄ and Au- and Ag-MnO hybrids.¹²⁸ Some interesting properties and applications of these unique nanoparticles will also be highlighted in following sections. In a slightly modified procedure, Fe₃O₄-quantum dot conjugates have also been developed. However, here the Fe₃O₄ nanoparticles act as the seeds for the growth of either CdS¹²⁶ or CdSe¹²⁹ quantum dots. Though these examples feature hybrid iron oxide and ferrite-based magnetic nanoparticles, there are also many interesting magnetic nanomaterials comprised of FePt nanoparticles.

The development of FePt-based hybrid nanoparticles involves some very interesting chemistry stemming from the Pt atoms in the alloyed seed nanoparticles. In one example, the FePt nanoparticles are capable of seeding the growth of Au nanoparticles through a catalytic reaction involving the absorption of hydrogen gas to the surface Pt atoms.¹¹⁷ Following absorption, the H atoms subsequently reduce solution phase Au⁺ ions to Au⁰ that subsequently “fuse” to the FePt nanoparticles resulting in the familiar dimeric architecture.¹¹⁷ In a different approach, it is also possible to utilize emulsion chemistry to seed the growth of Ag nanoparticles on the surface of FePt nanoparticle using so called “colloidosomes”.¹²³ In this process, the hybrid nanoparticles are generated following FePt nanoparticle dissolution in organic solvent and subsequent emulsification in an aqueous solution containing Ag⁺ atoms through ultrasonication. Because the surface ligands on the nanoparticle are labile, it is proposed that removal of these ligands during sonication exposes the nanoparticle surface atoms that are then able to catalyze the reduction of Ag⁺ to Ag⁰. The Ag⁰ atoms are deposited onto the nanoparticle surface as a Ag

nanoparticle that continues to grow as more Ag⁺ is subsequently reduced through continued sonication. This “colloidosome” approach is also useful for making Fe₃O₄-Ag and Au-Ag hybrid nanoparticles starting from hydrophobic Fe₃O₄ or Au nanoparticles, respectively.¹²³ FePt nanoparticles can also be the foundations for the growth of quantum dot-magnetic nanoparticle hybrids.

In the synthesis of such hybrids, FePt nanoparticles are first shelled with an amorphous layer of chalcogen (sulfur or selenium), which can be subsequently alloyed through the addition of a group 12 metal (Cd or Zn) resulting in an amorphous, metastable shell of the corresponding group 12 metal-chalcogenide.^{125,130,131} As the temperature is raised, the core@shell nanoparticles undergo a dewetting process due to the large lattice mismatch between the FePt and the group 12 metal sulfide resulting in dimeric nanoparticles with crystalline domains of FePt and CdS, CdSe or ZnS.^{130,131} Zanella also reported that FePt-PbS hybrids can be made through an identical procedure, but other dimeric nanoparticles such as FePt-ZnSe and FePt-PbSe could not be prepared as they were too unstable.¹³¹ Though both the FePt and quantum dot components of these nanoparticles are crystalline, little work has been carried out to learn about the interfacial region between the FePt and quantum dots; Zanella could find no evidence that the growth of the semiconductor crystals is epitaxial.¹³¹ As such, it is not clear how the face-centered cubic lattice of FePt and the quantum dots interact. In an analogous approach using γ -Fe₂O₃ rather than FePt, Kwon and Shim were able to shell γ -Fe₂O₃ nanoparticles with sulfur and subsequently add a group 12 metal (Zn, Cd and Hg) to generate the corresponding amorphous alloy.¹³² Much like Zanella¹³¹ and Xu,^{125,130} heating the core@shell nanoparticles induces dewetting and the formation of distinct domains of γ -Fe₂O₃ and ZnS, CdS or HgS. In these structures there is a direct correlation in the percent of lattice mismatch between the γ -Fe₂O₃ lattice and that of the CdS, ZnS and HgS nanoparticles and the number of quantum dots that are seeded on the surface of the γ -Fe₂O₃ nanoparticle. The percentage difference between dimensions of the lattices in the γ -Fe₂O₃ nanoparticles and the CdS, ZnS and HgS increases from 4.0 to 4.6 and 5.1%, respectively, and these differences are reflected in the number of seeds formed on the iron oxide nanoparticle (~ 1.45 to 1.1 to 0.9 seeds per nanoparticle, respectively) (Fig. 21).¹³²

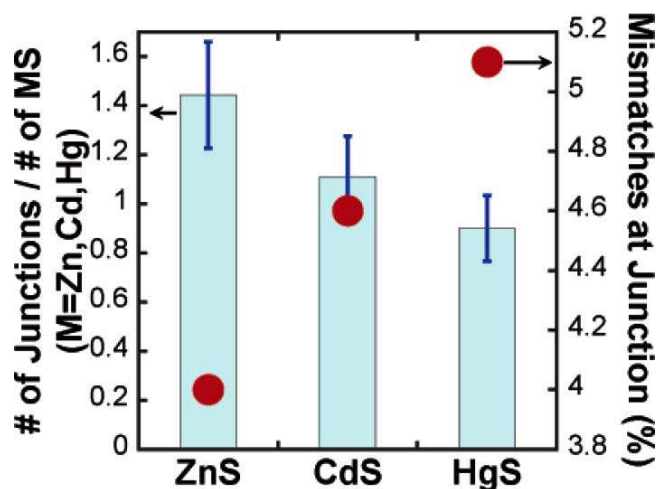


Fig. 21. Comparison of yield of heterojunction formation normalized to the number of hybrid nanoparticles with the average effective 2D lattice mismatch for the (111) γ - Fe_2O_3 /(111) ZnS, CdS, HgS. Bars are the number of normalized yields, and the filled circles are the effective mismatches. Reprinted with permission from Ref. 132. Copyright 2005 American Chemical Society.

FePt nanoparticles have also been utilized to seed the growth of Fe_xO_y (mixtures of Fe_3O_4 and Fe_2O_3) nanoparticles from standard nanoparticle precursors yielding FePt- Fe_xO_y hybrids.¹³³ The growth of these hybrid nanoparticles occurs most readily if the starting FePt nanoparticles are not purified, suggesting that the preparation of the nanoparticles may be mediated by residual Pt^{2+} ions. As the reaction is monitored by TEM analysis, it is evident that “flower-like”, multimetric structures are produced at intermediate stages, but the final product is a dimeric. This is analogous to the dewetting process proposed for the formation of FePt-quantum dot hybrids, but the Fe_xO_y “petals” are crystalline, suggesting that there is much to gain, thermodynamically speaking, for the coalescence of the Fe_xO_y into one node on the FePt surface rather than remaining dispersed over the entire surface. Again the authors found strong evidence that the growth of the Fe_xO_y nodes on the FePt seeds is epitaxial.

A number of very mild approaches have also been developed that can generate hybrid nanoparticles from reactions carried out under ambient conditions rather than through aggressive, high temperature routes. For example, Au nanoparticles can be grown on PbS nanoparticles under ambient conditions using dodecylamine to reduce gold from Au^{3+} to Au^0 .¹³⁴ The coalescence of Au^0 then

generates PbS-anchored Au nanoparticles. Though the gold nanoparticles are grown exclusively on the PbS nanoparticles, the interactions between the crystal lattices of the nanoparticle components do not have ordered orientations. In fact, the angles between the lattices in Au and PbS nanoparticles are variable and random suggesting that the growth of the hybrid nanoparticles is not epitaxial. It is possible in this case that the interactions between the two nanoparticles are mediated by Au-S interactions. In an analogous reaction, Au nanoparticles have been grown on ZnO nanoparticles again using an organic amine as the reducing agent.¹³⁵

4.1.2. Properties

4.1.2.1. Optical properties

The direct contact between two different materials with significantly different properties provides the opportunity to explore a number of very interesting properties and effects that each of the components could not possess on their own. For example, the nucleation of Fe_3O_4 on the surface of the Au nanoparticle causes a significant 18 nm red-shift in the plasmon absorption spectrum of the Au nanoparticle.¹²² This shift can be explained through a proposed deficiency in the electron population on the Au nanoparticle surface due to its coupling with the Fe_3O_4 nanoparticle.^{119,122} In fact both Yu and Shi suggest that the dimeric Au- Fe_3O_4 nanoparticles form exclusively because electron density is required to seed the growth of Fe_3O_4 on Au.^{119,122} This can also help explain the solvent effect on the architecture of hybrid nanoparticles. When π -electron rich solvents such as phenyl ether and benzyl ether are employed in the synthesis, the solvent can transiently replenish electron density to the Au core and facilitate the formation of additional Fe_3O_4 nanoparticles on its surface. Though somewhat damped by the presence of the Fe_3O_4 nanoparticles, these hybrid Au- Fe_3O_4 nanoparticles also exhibit a characteristic reflectance spectra in the 590–650 nm range, corresponding to the reflectance of similarly sized Au nanoparticles.¹²¹ In another example, hybrid Ag- Fe_3O_4 nanoparticles can undergo two-photon fluorescence emission from the Ag nanoparticle.¹¹⁸ In these examples, each of the nanomaterial components maintains its properties upon combining into a single nanoparticle. Unfortunately the incorporation of some nanoparticles into these hybrid nanostructures significantly hampers its performance.

Though some reports suggest that the photoluminescence properties of quantum dots anchored to FePt nanoparticles are essentially unaffected by the presence of the FePt nanoparticle,^{125,130} others have shown that the presence of the FePt nanoparticle both significantly dampens and shifts the photoluminescence emission from the CdS, CdSe, ZnS and PbS nanoparticles in the hybrid nanoparticle dimers.¹³¹ It is proposed that the underlying FePt nanoparticles act as electron and hole sinks, resulting in significantly decreased emission intensities for the resulting hybrid nanoparticles. Another strange optical property of these FePt–CdSe, FePt–CdS, FePt–ZnS and FePt–PbS is that the emission maxima of all of these dimers are centered at 460–490 nm, whereas the corresponding free quantum dot nanoparticles would have emissions at 713, 496, 337 and 3024 nm, respectively. Zanella *et al.* highlight that this is quite suspicious, and propose the emission could result from excess capping agent or even polymeric species formed during the synthesis of the hybrid nanoparticles.^{131,136} Hybrid Au–PbS nanoparticles do not exhibit unusual shifts in the photoluminescence emission maxima, but the intensity of the emission for Au–PbS is at least 30 times less intense than that for PbS.¹¹⁹ The decrease in luminescence intensity is attributed to the direct contact between the two nanoparticles, where the contact promotes charge separation via electron transfer from the PbS nanoparticles to the Au nanoparticle. In contrast to the hybrid nanoparticles prepared from FePt- and Au-quantum dots, Fe₃O₄–CdS and Fe₃O₄–CdSe hybrid nanoparticles exhibit improved, but still damped photoluminescence intensity.^{126,129} Selvan demonstrated not only an ability to make Fe₂O₃–CdS nanoparticles, but also that the size (and hence the emission properties) of the CdS nanoparticle component of the hybrid nanoparticles could be tuned.¹²⁶ These hybrid nanoparticles have quantum yields significantly higher than the corresponding FePt–CdS-based hybrids¹³¹ and the resulting nanoparticles can be readily functionalized and utilized in labeling and magnetic confinement assays (Fig. 22).

Though the direct attachment of most photoluminescent nanoparticles to FePt and Au nanoparticles results in a severe quenching of the photoluminescence, Wang demonstrated that the seeded growth of Au nanoparticles on ZnO nanoparticles in a procedure analogous to Yang¹³⁴ actually results in enhanced photoluminescence emission of the ZnO nanoparticle.¹³⁵ Though the explanation

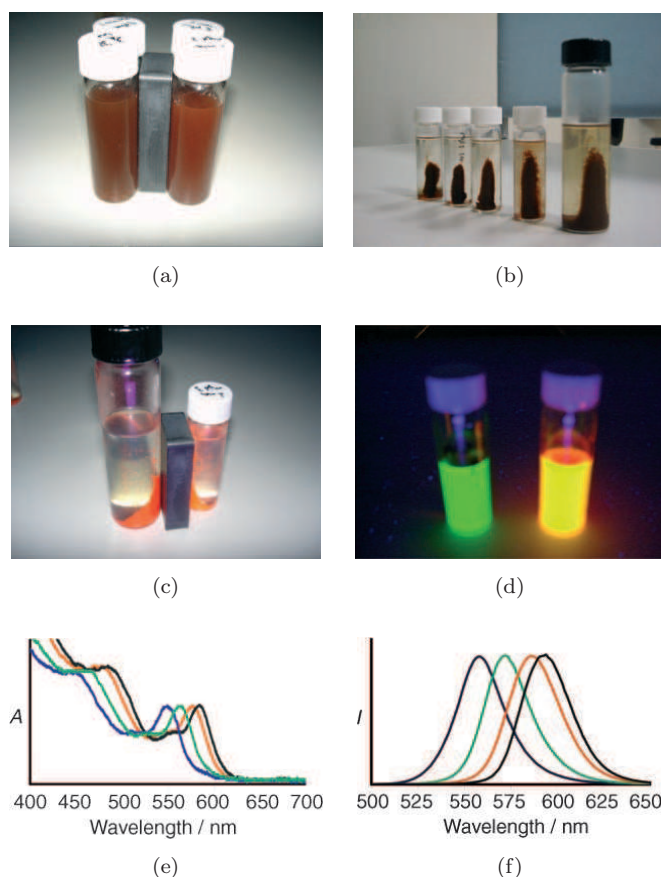


Fig. 22. Examples of how the Fe₃O₄–CdS nanoparticles can be magnetically confined (a) and (b), are luminescent (c) and (d) and how the emission can be tuned over a range of wavelengths (e) and (f). Reprinted with permission from Ref. 126. Copyright 2007 Wiley-VCH Verlag GmbH & Co. KGaA.

for this luminescence enhancement is complex, it mirrors the reasoning behind the shifts in the plasmon absorption of the Au nanoparticle following the growth of Fe₃O₄ on its surface.^{119,122} That is, the coupling of the Au nanoparticle directly to the ZnO nanoparticle results in a transfer of electrons from the gold nanoparticle to the ZnO nanoparticle, increasing the Fermi level energy and the electron density in the conduction band of the ZnO nanoparticle. It is also possible that there could be enhanced hole–electron recombination due to the interplay between the plasmon band of the Au nanoparticle and the emission of the ZnO nanoparticle. This interplay is proposed to enhance the localized electromagnetic field surrounding the ZnO nanoparticles, resulting in the two-fold enhancement in the multi-photon Raman scattering properties of these hybrid nanoparticles in comparison to ZnO nanoparticles alone.

In summary, following hybridization with FePt and Fe_3O_4 , the photoluminescence of quantum dots is normally decreased. This is attributed to electron or hole sink effects of these nanoparticles. However, when hybridized with Au, the photoluminescence behavior of quantum dots will also be affected by the interplay of plasmonic resonance and emission. This interplay is very interesting and will certainly be further investigated and eventually exploited in other applications.

4.1.2.2. Magnetic properties

The majority of focus on magnetic materials thus far has focused primarily on single component materials. Many of the nanoparticles highlighted thus far have magnetic components interfaced with magnetic and nonmagnetic components. As such, it is interesting to explore how the introduction of another material in direct contact with the surface of the magnetic nanoparticles affects their magnetic properties considering how important surface effects can be on the magnetic properties of nanomaterials. In the previous section it was shown that the presence of the iron oxide nanoparticles affects the surface plasmon properties of the gold nanoparticles, but it is also important to point out that the presence of the Au nanoparticle can affect the properties of the iron oxide nanoparticles as well.^{119,122,124} When the Fe_3O_4 nanoparticles are in direct contact with Au nanoparticles larger than them, the resulting coercivity and the magnetic field required to reach saturation magnetization increase and the saturation magnetization decreases significantly with respect to that of the analogous free Fe_3O_4 nanoparticle.^{119,122} In contrast, when the Au (or Ag) nanoparticles are significantly smaller than the Fe_3O_4 the magnetic properties of the conjugate are essentially identical to that of the Fe_3O_4 nanoparticle.^{118,122} These differences are attributed to both thermal agitation and spin canting¹³⁷ due to spin frustration and lattice strain in Fe_3O_4 nanoparticles in contact with the Au nanoparticles. This effect is specifically manifested at the surface of the nanoparticles, which is significantly affected by the presence of large Au nanoparticle, which have many surface plasmon electrons that can interfere with the magnetic properties of the Fe_3O_4 nanoparticles.^{138–140}

The magnetization curve for dimers of FePt and Au nanoparticles appears to be unaffected

by presence of the Au nanoparticle. In fact, the saturation magnetization is higher than that for similarly sized iron oxide nanoparticles (55 versus 40 emu/g Fe).¹¹⁷ In contrast, the intimate contact between the FePt nanoparticles and the quantum dots has an unusual effect on the magnetic properties of the FePt nanoparticles. With the exception of FePt–CdS, all other samples required exceedingly large fields to reach saturation magnetization (> 200 KOe).¹³¹ It is believed that the magnetization of these hybrids may be influenced by the diffusion of atoms into the FePt nanoparticle during synthesis.¹³¹

The development of FePt– Fe_xO_y nanoparticles allows the investigation of how combining hard (FePt) and soft (Fe_xO_y) magnets into a single architecture affects the magnetic properties.¹³³ As these materials are combined, changing the volume fraction of the FePt versus Fe_xO_y components of the hybrid nanoparticles actually allows one to tune the magnetic behavior of the material. Specifically, as the volume fraction of the Fe_xO_y component is increased, the coercivity of the hybrid can be decreased. Of course, the opposite is also true. This unique magnetic property was also demonstrated in another hybrid nanoparticle with the same composition, but with a core@shell architecture (i.e., FePt@ Fe_3O_4).¹⁴¹ It is also noteworthy that these FePt– Fe_xO_y nanoparticles show promise in model proton nuclear relaxation studies, suggesting that they could be employed as effective MRI contrast agents.¹³³

A magneto-optical study involving dimers of Ag nanoparticles bound to ferromagnetic CoFe_2O_4 nanoparticles ($\text{Ag-CoFe}_2\text{O}_4$) shows enhanced Faraday rotation of the Ag containing nanoparticles in comparison to the monomeric CoFe_2O_4 nanoparticles.¹²⁴ Although the magnitude of the Faraday rotation is decreased, the magneto-optical response for the Ag containing nanoparticles is significantly higher than that for the monomeric nanoparticles as the Faraday rotation is measured at wavelengths greater than 633 nm. This “crossover” is explained by noting that at these wavelengths the Ag-plasmon band is irradiated to a greater extent than the CoFe_2O_4 component. As such, there is a strong contrast in spectral behavior that is attributed to the dielectric contribution of the Ag-nanoparticle component in the Ag– CoFe_2O_4 dimer, which appears to lead to an increase in the magneto-optical response of the hybrid nanoparticle. Importantly

this effect is totally absent in monomeric CoFe_2O_4 nanoparticles.

MRI contrast is another interesting property inherent to many of these hybrid magnetic nanoparticles. Iron oxide is extensively utilized as an MRI contrast agent, and Xu demonstrated that $\text{Au-Fe}_3\text{O}_4$ nanoparticles are capable of providing effective T_2 weighted MRI contrast, though these nanoparticles are slightly less effective as the homogeneous Fe_3O_4 nanoparticles themselves.¹²¹ More recently MnO nanoparticles have been developed for T_1 -weighted MRI contrast agents. Analogous to Xu, Choi was able to demonstrate that the presence of Au on the Fe_3O_4 and MnO nanoparticles had little effect on the T_1 - and T_2 -relaxation times of the resulting nanoparticles. Further, the specific relaxivities of the nanoparticles compare quite favorably to those of the homogenous nanoparticles with no Au component (Fig. 23).¹²⁸

4.1.2.3. Surface properties

The ability to tune the functionality of the dimeric nanoparticle based on the composition of the nanomaterial provides an avenue to develop functional nanoprobe for biodiagnostic applications. For example, it is well known that thiols and disulfides have strong affinities for Au and Ag surfaces, whereas dopamine and carboxylic acid derivatives bind strongly to iron oxide. This selective surface modification is nicely demonstrated for $\text{Fe}_3\text{O}_4\text{-Ag}$ hybrids where each nanoparticle component can be

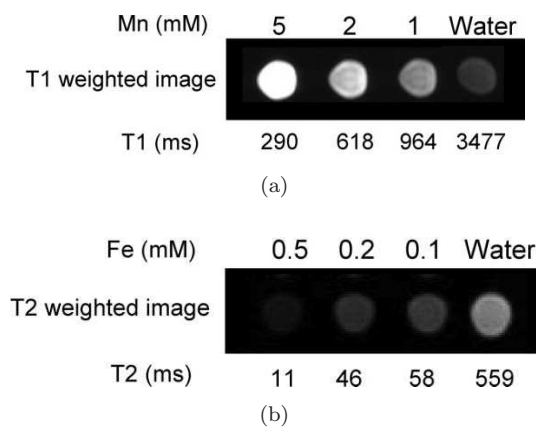


Fig. 23. (a) T_1 -weighted images and relaxation times at various concentrations of Au-MnO heterodimer nanoparticles and (b) T_2 -weighted images and relaxation times at various concentrations of $\text{Au-Fe}_3\text{O}_4$ heterodimer nanoparticles. Reprinted with permission from Ref. 128. Copyright 2008 American Chemical Society.

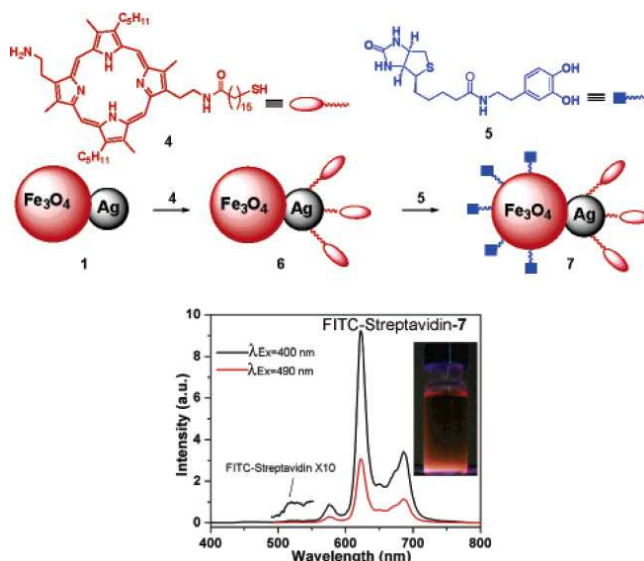


Fig. 24. The selective modification of the Fe_3O_4 and Ag portions of the hybrid nanoparticle with modified dopamines and thiols, respectively and the fluorescent spectra of the modified $\text{Fe}_3\text{O}_4\text{-Ag}$ hybrid nanoparticle and the corresponding fluorescent images were obtained using a UV lamp with the wavelength centered at 365 nm. Reprinted with permission from Ref. 123. Copyright 2005 American Chemical Society.

independently functionalized.¹²³ That is, the Fe_3O_4 component can be functionalized with a biotin-modified dopamines and the Ag component can be functionalized with porphyrin-modified thiols. The resulting nanoparticles are hydrophilic, fluorescent, can bind to specific targets and are magnetically responsive (Fig. 24). With all of these attributes, this architecture shows incredible promise for biodiagnostic and imaging applications.¹²³ This selective surface modification has also led to the development of $\text{Ag-Fe}_3\text{O}_4$ nanoparticles for cell labeling and imaging. Such nanoparticles can be made hydrophilic through the selective modification of the Ag surface with tiopronin (a thiolated tripeptide) and the resulting nanoparticles are readily endocytosed by macrophage cells. In this case the Fe_3O_4 nanoparticles can be left bare, where the resulting Fe-O^- groups on the surface that impart solubility due to their hydrophilic nature and electrostatic repulsion.¹¹⁸

4.1.3. Applications

The combination of magnetic responsivity and imaging modalities makes the aforementioned hybrid nanoparticles extremely valuable as biological imaging probes. $\text{Au-Fe}_3\text{O}_4$ nanoparticles have recently been utilized for the multimodal imaging

of cells that are overexpressing a protein called epidermal growth factor receptor (EGFR), which is a potential marker for lung and breast cancers.¹²¹ Following selective surface modification of the Fe_3O_4 portion of the nanoparticle with an antibody and the Au portion with a thiol-modified polyethylene glycol, the hybrid nanoparticles were able to selectively interface with EGFR-positive target cells, and the labeled cells could be identified based on enhanced MRI T_2 contrast from the Fe_3O_4 nanoparticle and strong reflection spectra that can be easily observed with a confocal microscope from the Au nanoparticles (Fig. 25).

In an alternative strategy, Ag- Fe_3O_4 nanoparticles were used for the magnetic manipulation and detection of macrophage cells through the two-photon fluorescence inherent to the Ag nanoparticle in the hybrid.¹¹⁸ The nanoparticles were surface modified such that they were readily endocytosed by macrophage cells and the labeled macrophages can be fluorescently imaged through the two-photon excitation of the Ag nanoparticles with femtosecond pulses of 900 nm light (Fig. 26). The cells can also be magnetically manipulated with a rare earth magnet, so the combination of these nanoparticles into one dimeric structure represents a potentially powerful approach to sort and identify cells via magnetic manipulation and Ag-based two-photon fluorescence detection.

FePt-Au dimer nanoparticles have been exploited in dual-mode imaging applications where the Au nanoparticle can be used for silver stain-based detection and the FePt nanoparticles can enhance

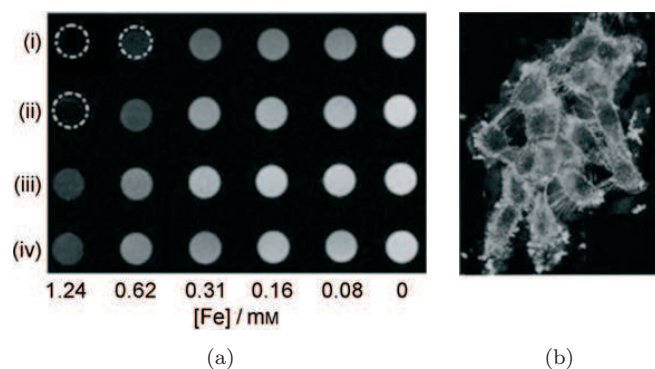


Fig. 25. (a) T_2 -weighted MRI images of (i) 20-nm Fe_3O_4 , (ii) 3-20-nm Au- Fe_3O_4 , (iii) 8-20-nm Au- Fe_3O_4 nanoparticles, and (iv) A431 cells labeled with 8-20-nm Au- Fe_3O_4 nanoparticles. (b) Reflection images of the A431 cells labeled with 8-20-nm Au- Fe_3O_4 nanoparticles. Reprinted with permission from Ref. 121. Copyright 2008 Wiley-VCH Verlag GmbH & Co. KGaA.

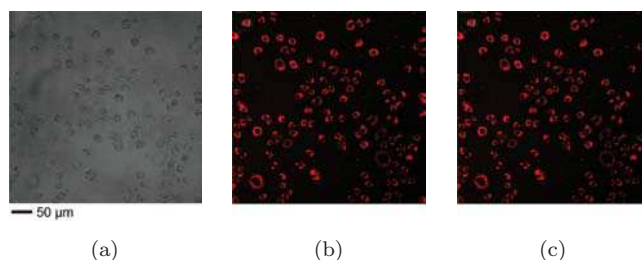


Fig. 26. (a) Transmission, (b) two-photon fluorescence, and (c) overlaid images of macrophage cells incubated with Fe_3O_4 -Ag heterodimer nanoparticles. The red is the two-photon fluorescence image from the Ag portion of the nanoparticles labeling the cells. Excitation laser wavelength of 900 nm. Reprinted with permission from Ref. 118. Copyright 2008 Wiley-VCH Verlag GmbH & Co. KGaA.

contrast in MRI-based imaging.¹¹⁷ These detection strategies were demonstrated in two assays. In the first, the Au nanoparticle can participate in a sandwich immuno-assay to identify the presence of a biomolecule. Within such an assay, when the nanoparticles are anchored to a surface through a specific interaction, a catalytic reduction of added silver ions onto the Au nanoparticles can signal the presence of an antigen. Conversely, the nanoparticles can be decorated with antibodies that can recognize polysialic acid (a cancer biomarker on cells). Upon specific attachment to cells expressing this biomarker, the cells can be identified via MRI contrast enhancements provided by the FePt portion of the nanoparticle.¹¹⁷ Another excellent example of dual mode identification was demonstrated through the use of hybrid nanoparticles for the detection of single stranded DNA in solution.¹²⁸ Au- Fe_3O_4 nanoparticles were modified with single stranded DNA, incubated with a complementary strand of DNA and the selective hybridization of the complementary DNA could be identified based on (1) a size increase of the nanoparticles via dynamic light scattering because of hybridization induced aggregation, (2) a broadening and shift in the UV-vis absorption spectrum of the plasmon band of the Au portion of the nanoparticle (again due to DNA-induced nanoparticle aggregation) and (3) an increase in the T_2 -relaxation time of the Fe_3O_4 nanoparticle following hybridization-mediated aggregation of the nanoparticles (Fig. 27).

In a potential nanoparticle-based detection/delivery platform that makes use of both the magnetic and luminescent components in an Fe_3O_4 -CdSe nanoparticle, Gao modified the surface of their hybrid nanoparticles with a peptide called

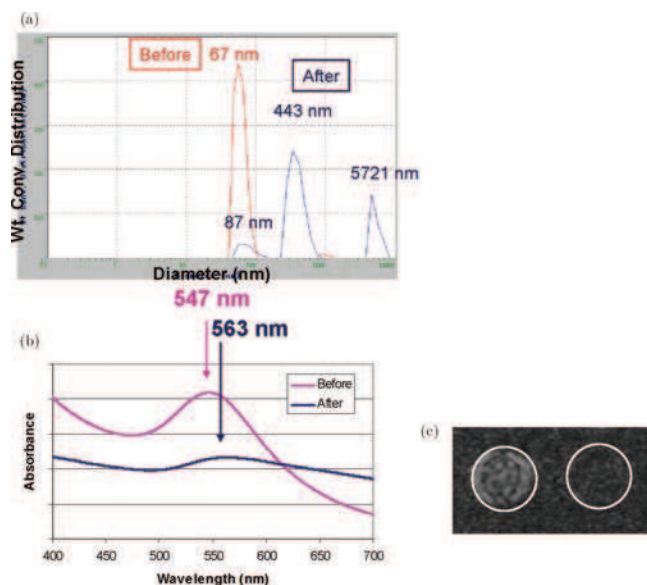


Fig. 27. The Au-Fe₃O₄ hybrid nanoparticle response to DNA hybridization, where, hybridization is signaled by (a) a change of size by dynamic light scattering; (b) a change of plasmon absorption from the Au component and (c) a change of contrast in *T*₂-weighted MRI from the Fe₃O₄ component. Reprinted with permission from Ref. 128. Copyright 2008 American Chemical Society.

glutathione allowing the nanoparticles to not only disperse in aqueous solution, but it also allowed them to be endocytosed by human embryonic kidney (HEK293T) cells.¹²⁹ Following endocytosis, the location of the Fe₃O₄-CdSe could be determined based on photoluminescence imaging, and the authors demonstrated that it was possible to magnetically manipulate the nanoparticles within the cells. Through a combination of magnetic manipulation and photoluminescent imaging it was demonstrated that the nanoparticles could be localized to specific locations within the cell for potential delivery of a drug or therapeutic agents (Fig. 28).

4.2. Core@shell nanoparticles

In the previous section, severe lattice mismatches between different nanoparticles led to the dewetting and the generation of hybrid nanoparticles with dimeric or multimeric segregated structures where the nanoparticles were coupled through minimal surface contact. In this section, a series of fascinating nanoparticles with core@shell architectures will be presented. In these examples, the development of synthetic techniques designed to preserve intimate contact between the different materials will be discussed. In general this approach requires the

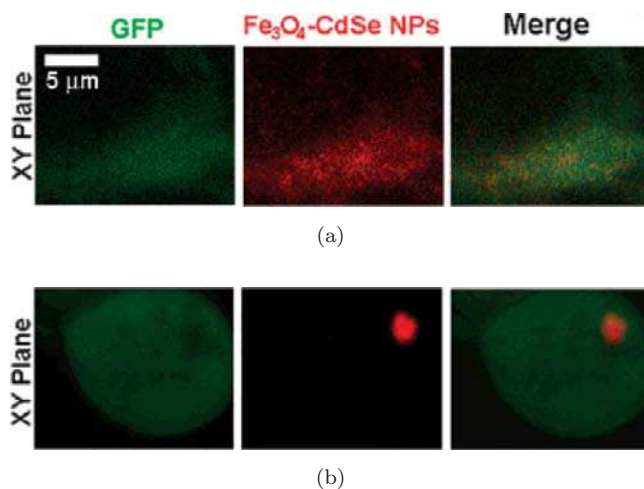


Fig. 28. A demonstration of the magnetic manipulation of the Fe₃O₄-CdSe nanoparticles within the cell. The green fluorescent protein within the cell does not move under magnetic manipulation, whereas the red emission from the Fe₃O₄-CdSe is concentrated to the upper corner of the cell upon placement of a rare-earth magnet in this location. This demonstrates that such nanoparticles could potentially deliver substrates or drugs to specific compartments of a cell under magnetic manipulation. Reprinted with permission from Ref. 129. Copyright 2008 American Chemical Society.

use of nanomaterials with lattice dimensions that are quite similar. In addition to the synthetic protocols, we will also highlight some interesting properties that the resulting nanoparticles possess and introduce some applications that can be carried out with functional core@shell nanoparticles.

4.2.1. Synthesis

One of the most practical approaches to the generation of core@shell materials involves the oxidation of a reactive nanoparticle under ambient conditions. Lee¹⁴² and Somaskandan¹⁴³ successfully utilized this approach to prepare Ni@NiO and Fe@Fe_xO_y nanoparticles, respectively. In each case the reactive core material (Ni and Fe, respectively) was synthesized under inert, high temperature conditions in organic solvents. Upon exposure to air, both of these nanoparticles oxidize controllably from the surface inward, resulting in core@shell nanoparticles with superparamagnetic properties. Fe@Fe_xO_y nanoparticles have also been prepared through the controlled oxidation of Fe nanoparticles mediated by (CH₃)₃NO, an oxygen transferring agent.¹⁴⁴ Both Peng and Somaskandan prepared Fe@Fe_xO_y nanoparticles with amorphous Fe cores and crystalline shells that stabilize the Fe amazingly well under ambient conditions.^{143,144} These

nanoparticles are also interesting because they are comprised of two magnetic materials (i.e., Fe and Fe_xO_y). Another example of such a hybrid nanoparticle was demonstrated by Zeng, where the surface of FePt nanoparticles could be controllably modified with Fe_3O_4 shells (0.5–3.0 nm) through the growth of the shell on pre-existing FePt nanoparticles.¹⁴¹ It is noteworthy that rather subtle changes in a synthetic protocol can lead to either dimeric¹³³ or core@shell structures.¹⁴¹ TEM analysis of the FePt@ Fe_3O_4 nanoparticles suggests that the growth of the Fe_3O_4 shell is epitaxial, where the crystalline phases of the FePt core align quite well with the lattice phases of the Fe_3O_4 shell.

An alternative strategy to construct a shell around a given nanoparticle involves the coalescence of preformed nanoparticles onto the surface of an existing nanoparticle. Zhang was able to develop core@shell nanoparticles comprised of Fe@Au through a process in which gold nanoparticles (80 nm) were irradiated at 532 nm with a pulsed laser beam in the presence of zero valent iron nanoparticles.¹⁴⁵ It is proposed that the irradiation of the Au nanoparticles heats them to the point that they essentially melt and fuse to the surface of the Fe seed nanoparticles, forming a nonporous shell surrounding the core. Core@shell nanoparticles can also be prepared through a similar heterocoalescence of Au nanoparticles on the surface of iron oxide nanoparticles simply through heating to 149°C.¹⁴⁶ Both Zhang and Park are able to develop these nanoparticles because of the unique properties inherent to nanosized gold, where it is proposed that the melting point of nanoparticles of this size is significantly depressed with respect to the bulk material.^{145,146} It is this property that allows the melting and coalescence of the Au nanoparticles onto the surfaces of the Fe and Fe_xO_y nanoparticles, respectively.

Following a simple and very gentle procedure, Au^{3+} ions can be reduced to Au^0 and subsequently form a shell on the surface of Fe_3O_4 nanoparticles in a room temperature synthesis facilitated by oleylamine (the reducing agent for Au^{3+}).¹⁴⁷ The resulting Fe_3O_4 @Au nanoparticles, where the Au shell is only 1 nm thick can be subsequently transferred to an aqueous solution through the addition of sodium citrate and CTAB. Following phase transfer, the composition and thickness of the metal shell can be controllably tuned through the addition of Au^{3+} or Ag^+ ions. The resulting nanoparticles can have compositions ranging from Fe_3O_4 @Au, where

the Au shell is 3 nm thick, to Fe_3O_4 @Au@Ag where the Au shell is 1 nm thick and the Ag shell is 2 nm thick. This reaction strategy can also be utilized to prepare core@shell Co@Au nanoparticles, where an organic modified Co nanoparticle is encapsulated in a Au shell through the reduction of gold atoms on the surface of the Co nanoparticle by oleylamine.¹⁴⁸

Another interesting approach to the preparation of core@shell nanoparticles is the development of redox-transmetalation chemistry on Co nanoparticles.¹⁴⁹ The development of transmetalation chemistry eliminates the need to nucleate a shell material on an existing nanoparticle or the “fusion” of two nanoparticle materials. Instead, the process is driven by a spontaneous redox reaction between solution phase metal ions (Pt, Au, Pd or Cu) and Co atoms on the surface of an existing nanoparticle (Fig. 29).¹⁴⁹ During the transmetalation process surface atoms undergo sacrificial oxidation as incoming Pt^{2+} , Au^{3+} , Pd^{2+} or Cu^{2+} are reduced and subsequently replace the existing Co atoms in the nanoparticle. This process is primarily driven by the thermodynamically favorable standard potential values for each redox process (i.e., $3\text{Co}^0 + 2\text{Au}^{3+} \rightarrow 3\text{Co}^{2+} + 2\text{Au}^0$). Though the redox-transmetalation reaction works quite well for Lee and coworkers, there are reports where hollow gold shells have been prepared through similar reactions through the Kirkendall effect.^{150–152} In these reactions a unique solid state diffusion process (the Kirkendall effect) would actually build a Au shell around the Co-nanoparticle, and the nanoparticle would only act as a sacrificial template for the formation of the shell as described in the following paragraph.

Xu demonstrated two excellent examples of unique nanoparticle structures that utilize the Kirkendall effect to produce yolk@shell architectures.^{153,154} In contrast to a solid core@shell structure, the yolk@shell structure contains a core that is not attached to the shell, an architecture

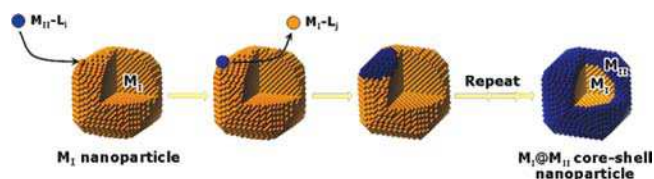


Fig. 29. Schematic of core@shell nanoparticle formation via redox transmetalation processes. Reprinted with permission from Ref. 149. Copyright 2005 American Chemical Society.

somewhat reminiscent of a rattle. In a process analogous to that pioneered by Yin to synthesize hollow cobalt sulfide and cobalt oxide nanoparticles,⁶⁶ FePt nanoparticles were first encapsulated in a shell of cobalt or iron to yield FePt@Co¹⁵⁴ or FePt@Fe¹⁵³ nanoparticles, respectively. The FePt@Co nanoparticles can be subsequently reacted with sulfur to generate a nonattached CoS₂ shell (i.e., FePt@CoS₂ yolk@shell architecture) and FePt@Fe nanoparticles can be oxidized at room temperature to yield a yolk@shell structure of FePt@Fe₂O₃. The resulting rattle-like FePt@CdS₂ and FePt@Fe₂O₃ nanoparticles can be modified such that the nanoparticles become water soluble and they are shown to be readily endocytosed by cells.^{153,154} Shevchenko *et al.* have also demonstrated that yolk@shell structures of Au@Fe_xO_y can be prepared through the *in situ* generation of Au@Fe core@shell nanoparticles and their subsequent oxidation by air.¹⁵⁵ The Kirkendall effect results in solid state diffusion similar to that described by Gao, where a nonattached shell of Fe_xO_y is generated around the Au core. These exciting new yolk@shell structures are produced primarily because there are significantly different diffusion rates for the different atoms throughout the solid matrix. For example, Gao and Shevchenko proposed that yolk@shell structures are generated because oxygen and iron have different diffusion rates through the outer shell.^{153,155}

4.2.2. Properties

4.2.2.1. Optical properties

The Fe₃O₄@Au nanoparticles described by Xu display a prominent plasmon absorption, which is uncommon for such thin Au layers.¹⁴⁷ The enhanced SPR intensity is attributed to the increased charge on the surface due to the presence of the citrate and CTAB ions. As the composition of the nanoparticles is changed, the SPR band can be concomitantly tuned through the addition of Au³⁺ or Ag⁺ ions which results in the red or blue shifting of the plasmon band, respectively as the metal is reduced onto the Fe₃O₄@Au surface. More specifically, the SPR band can be red shifted to 561 nm as the Au shell is tuned to 3 nm, or blue-shifted to 501 nm as the shell is coated with 2 nm of Ag (Fig. 30). A similar blue shift was observed as increasingly thicker Ag shells are constructed around Au nanorods.¹⁵⁶

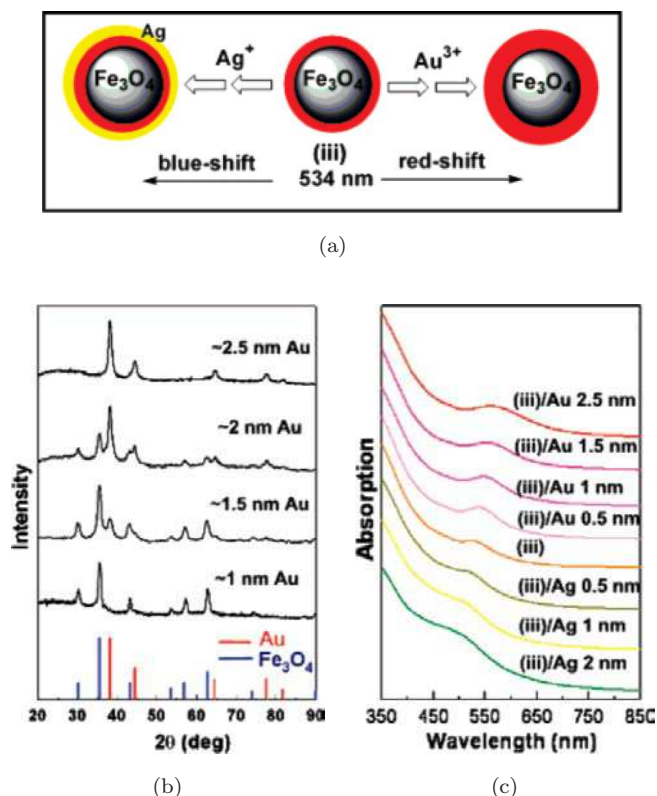


Fig. 30. (a) Schematic illustration of the formation of Fe₃O₄@Au and Fe₃O₄@Au@Ag and the control on the plasmonic properties; (b) XRD of the Fe₃O₄/Au nanoparticles with various Au coating thickness; (c) UV-Vis absorption spectra of the Fe₃O₄@Au and Fe₃O₄@Au@Ag demonstrating the plasmon shifts with composition of the nanoparticle and shell thickness. Reprinted with permission from Ref. 147. Copyright 2007 American Chemical Society.

4.2.2.2. Magnetic properties

The development of core@shell nanoparticles are very interesting as these nanostructures provide the ability to investigate how two magnetic materials can be combined and how the mixing of the different materials affects the magnetic properties of the resulting conjugate. In addition, these architectures also provide the opportunity to investigate and develop stabilized samples of highly reactive nanomaterials with high magnetic moments. This is exemplified by Zhang in the development of superparamagnetic Fe@Au nanoparticles.¹⁴⁵ The gold shell was shown to be nonporous and capable of preventing oxidation of the highly reactive Fe core for months. In addition, the magnetic moment of nanoparticles is reported to be 210 emu/g Fe, which is ~96% of the value for bulk Fe.¹⁴⁵ Another example of nanoparticles incorporating a stabilized derivative of zero valent iron was reported

independently by Somaskandan¹⁴³ and Peng.¹⁴⁴ Here the $\text{Fe}@\text{Fe}_x\text{O}_y$ nanoparticles show high magnetic moments (127 and 103 emu/g Fe, respectively) and excellent long term stability. It is noteworthy that Fe_3O_4 nanoparticles have magnetic moments of ~ 80 emu/g Fe, so the introduction of zero valent Fe into these nanoparticles significantly improves the saturation magnetization values.

Analogous to the dimeric versions of $\text{FePt}-\text{Fe}_x\text{O}_y$ described in Sec. 4.1.2.2, the incorporation of both FePt and Fe_3O_4 into a single core@shell nanoparticle is interesting as it combines a hard magnet (FePt, high coercivity) and a soft magnet Fe_3O_4 (low coercivity).¹⁴¹ Zeng was able to demonstrate that the magnetic properties, specifically the coercivity of the nanoparticles, can be tuned by changing the thickness of the Fe_3O_4 shell on the FePt nanoparticle core.¹⁴¹ The development of these nanoparticles allowed the authors to elucidate that the coercivity of $\text{FePt}@\text{Fe}_3\text{O}_4$ nanoparticles is dependent on the volume ratios of the two components, and not necessarily the thickness of the shell material as earlier predicted.¹⁴¹ This is an excellent example of how the synthesis of a unique material provided otherwise unattainable knowledge, and demonstrates the power of creating new and interesting nanomaterial architectures.

Gao demonstrated that yolk@shell nanoparticles exhibit magnetic properties that are unique in comparison to the analogous core@shell structure and that hollow nanostructures provide enhanced magnetic resonance imaging contrast in comparison to traditional solid nanoparticles.¹⁵³ Investigating a series of nanoparticles including $\text{FePt}@\text{Fe}_2\text{O}_3$ yolk@shell, $\text{FePt}@\text{Fe}_3\text{O}_4$, $\text{Pt}@\text{Fe}_2\text{O}_3$ yolk@shell and hollow Fe_2O_3 nanoparticles shows that all of these nanoparticles are superparamagnetic, but that the magnetic moment for $\gamma\text{-Fe}_2\text{O}_3$ hollow nanoparticles is significantly higher (50.8 emu/g) than that for the rest of the nanoparticles (i.e., $\text{FePt}@\text{Fe}_2\text{O}_3$ yolk@shell, $\text{FePt}@\text{Fe}_3\text{O}_4$ and $\text{Pt}@\text{Fe}_2\text{O}_3$ yolk@shell nanoparticles have magnetic moments of 25.2, 24.8 and 19.5 emu/g, respectively). Though the magnetic moments of the $\text{FePt}@\text{Fe}_2\text{O}_3$ yolk@shell, $\text{Pt}@\text{Fe}_2\text{O}_3$ yolk@shell and $\text{FePt}@\text{Fe}_3\text{O}_4$ nanoparticles are nearly identical, it is interesting that the corresponding transverse relaxivities (r_2^*) are significantly different. These values are important because the r_2^* value is directly related to the ability for a material to enhance magnetic resonance imaging contrast. In accord with the mass magnetization

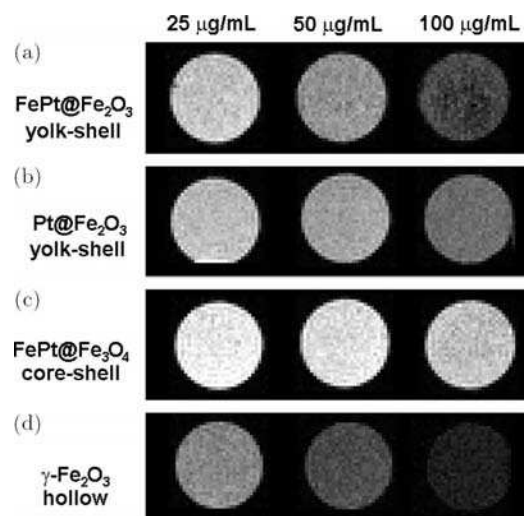


Fig. 31. T_2^* -weighted MR images of (a) $\text{FePt}@\text{Fe}_2\text{O}_3$ yolk@shell nanoparticles, (b) $\text{Pt}@\text{Fe}_2\text{O}_3$ yolk@shell nanoparticles, (c) $\text{FePt}@\text{Fe}_3\text{O}_4$ core@shell nanoparticles, and (d) $\gamma\text{-Fe}_2\text{O}_3$ hollow nanoparticles from a 7.0 T MRI system at 25, 50, and 100 $\mu\text{g/mL}$ in water (containing 1% agarose gel). Reprinted with permission from Ref. 153. Copyright 2008 American Chemical Society.

values, $\gamma\text{-Fe}_2\text{O}_3$ hollow nanoparticles exhibit the strongest MR signal attenuation effect, but the $\text{FePt}@\text{Fe}_2\text{O}_3$ and $\text{Pt}@\text{Fe}_2\text{O}_3$ yolk@shell nanoparticles are significantly better than the $\text{FePt}@\text{Fe}_3\text{O}_4$ core@shell nanoparticles (Fig. 31). Modulating the spin-spin relaxation processes of water protons surrounding the nanoparticles is particularly important for MRI contrast. Because the hollow and yolk@shell nanoparticles can fill with water, the interfacial region in contact with water in these nanoparticles should be much larger than that for solid nanoparticles at similar concentrations. The authors suggest that this could explain the observed enhancement in MR contrast/unit weight and is proposed to be why these hollow and yolk@shell structures produce the best MRI image contrast in all examples investigated. These results are quite powerful and suggest that hollow magnetic nanoparticles may exhibit advantages in MR relaxation enhancement due to their unique geometry that may be the focal point for new nanomaterials to aid in MRI imaging.

4.2.3. Applications

Biodiagnostic applications are a target that many believe could benefit the most from the development of multifunctional, hybrid nanoparticles. Lee,¹⁴² Somaskandan¹⁴³ and Peng¹⁴⁴ are interested in

incorporating their nanoparticles into biodiagnostic applications and were able to exchange the organic ligands on the surface of the original nanoparticles with hydrophilic ligands and impart water solubility to their nanoparticles. Further, Lee demonstrated that the Ni@NiO nanoparticles could be utilized to selectively interact with green fluorescent protein modified with polyhistidine and selectively magnetically confine this protein (Fig. 32).¹⁴² It is proposed that the strong attachment of proteins through coordinate bonds with the polyhistidine and Ni atoms on the surface of the nanoparticles should lead to the development of some novel biodiagnostic materials. The Fe₃O₄@Au nanoparticles developed by Park can be surface modified with targeting biomolecules and incorporated into magnetic confinement-surface enhanced Raman scattering identification-based biodiagnostic assays.¹⁴⁶ This was demonstrated in a magnetic confinement assay for a nanoparticle modified with protein A. Following the introduction of an IgG antibody-modified Fe₃O₄@Au nanoparticle, the protein A-decorated nanoparticle can be selectively interfaced to the Fe₃O₄@Au nanoparticles, leading to their magnetic confinement.

The unique yolk@shell nanoparticles developed by Xu show a number of very interesting biological applications.^{153,154} For example, the FePt@CoS₂ yolk@shell nanoparticles can be readily endocytosed by cells. The CoS₂ shell is quite porous and can easily fill with water. Because the environment within cells is acidic, the FePt nanoparticles encapsulated within the CoS₂ shell are susceptible to oxidation and decomposition to ionic Fe²⁺ and Pt²⁺ ions.¹⁵⁴ The released Pt²⁺ ions are subsequently able to migrate to the cell nucleus and damage DNA through the coordination to the 5'-GG-3' bases and the resulting inhibition of replication (Fig. 33).^{157–159} As such, these nanoparticles have been utilized to deliver a lethal dose of Pt²⁺ to cells, as demonstrated through the FePt@CoS₂ induced death of HeLa cells incubated with quite low concentrations of the nanoparticles



Fig. 32. Purification of His-tagged proteins from mixed solutions. Reprinted with permission from Ref. 142. Copyright 2006 American Chemical Society.

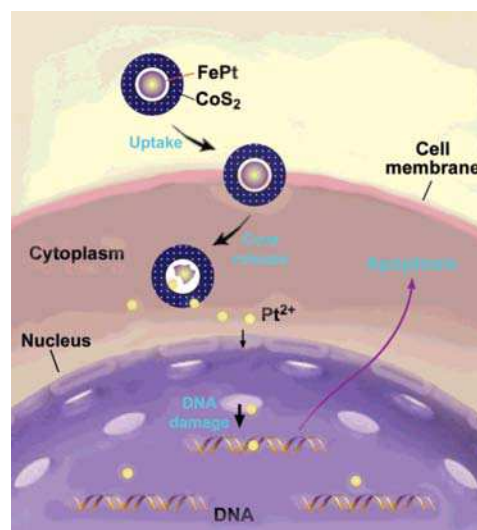


Fig. 33. Illustration of a possible mechanism accounting for FePt@CoS₂ yolk-shell nanocrystals killing HeLa cells. After cellular uptake, FePt nanoparticles were oxidized to give Fe³⁺ (omitted for clarity) and Pt²⁺ ions (yellow). The Pt²⁺ ions enter into the nucleus (and mitochondria), bind to DNA and prevent it from replicating which leads to apoptosis of the HeLa cell. Reprinted with permission from Ref. 154. Copyright 2007 American Chemical Society.

(< 2 µg/mL).¹⁵⁴ In addition to the use of these nanoparticles as drug delivery vehicles, they can also act as bimodal imaging/drug delivery probes. Following surface modification with a dopamine derivative, FePt@Fe₂O₃ yolk@shell nanoparticles can act as effective MRI contrast agents.¹⁵³ Akin to the FePt@CdS₂ nanoparticles described above, these nanoparticles also demonstrated an ability to be endocytosed by cells, allowing the FePt nanoparticles to decompose in the acidic cell environment and deliver Pt²⁺ ions that are capable of selectively killing the host cells. However, the FePt@Fe₂O₃ nanoparticles are slightly less toxic than the FePt@CoS₂ nanoparticles.

5. Conclusion

The recent research and development of the nanoparticles with special morphologies, e.g., with hollow interiors and branched structures, and multifunctional nanoparticles are outlined in this review. Despite the rapid advancement in these fields, the controlled synthesis of these nanostructures made of diverse materials and those with even higher structural complexity and hierarchical order still represent a significant challenge and will continue to be a hot and important research topic in the field of

nanoscience. Novel properties and associated “new physics” are expected to arise from these studies, which will enable the exploration and realization of advanced applications of these nanomaterials in various important fields such as biomedicine, catalysis, solar cells, nanoelectronics and so on. Although so far, the reports on these “practical” aspects are still quite limited, the huge potential of these nanostructures have been well appreciated, which should be realizable if great minds from multidisciplinary fields are combined.

References

1. T. S. Ahmadi, Z. L. Wang, T. C. Green, A. Henglein and M. A. El-Sayed, *Science* **272**, 1924 (1996).
2. A. P. Alivisatos, *Science* **271**, 933 (1996).
3. N. Chestnoy, R. Hull and L. E. Brus, *J. Chem. Phys.* **85**, 2237 (1986).
4. G. Schmidt, *Chem. Rev.* **92**, 1709 (1992).
5. M. L. Steigerwald and L. E. Brus, *Acc. Chem. Res.* **23**, 183 (1990).
6. H. Liang, H. Zhang, J. Hu, Y. Guo, L. Wan and C. Bai, *Angew. Chem. Int. Ed.* **43**, 1540 (2004).
7. Y. Sun, B. Mayers and Y. Xia, *Adv. Mater.* **15**, 641 (2003).
8. Y. Wang, P. Chen and M. Liu, *Nanotechnology* **19**, 045607 (2008).
9. F. Kim, J. H. Song and P. Yang, *J. Am. Chem. Soc.* **124**, 14316 (2002).
10. R. J. Nikhil, *Small* **1**, 875 (2005).
11. X. Peng, L. Manna, W. Yang, J. Wickham, E. Scher, A. Kadavanich and A. P. Alivisatos, *Nature* **404**, 59 (2000).
12. K. K. Caswell, C. M. Bender and C. J. Murphy, *Nano Lett.* **3**, 667 (2003).
13. Y. Sun, B. Gates, B. Mayers and Y. Xia, *Nano Lett.* **2**, 165 (2002).
14. M. Maillard, P. Huang and L. Brus, *Nano Lett.* **3**, 1611 (2003).
15. J. E. Millstone, S. Park, K. L. Shuford, L. Qin, G. C. Schatz and C. A. Mirkin, *J. Am. Chem. Soc.* **127**, 5312 (2005).
16. Y. Sun and Y. Xia, *Science* **298**, 2176 (2002).
17. Y. Xiong and Y. Xia, *Adv. Mater.* **19**, 3385 (2007).
18. S. M. Humphrey, M. E. Grass, S. E. Habas, K. Niesz, G. A. Somorjai and T. D. Tilley, *Nano Lett.* **7**, 785 (2007).
19. L. Manna, D. J. Milliron, A. Meisel, E. C. Scher and A. P. Alivisatos, *Nat. Mater.* **2**, 382 (2003).
20. D. J. Milliron, S. M. Hughes, Y. Cui, L. Manna, J. Li, L. Wang and A. P. Alivisatos, *Nature* **190**, 430 (2004).
21. J. Chen, D. Wang, J. Xi, L. Au, A. Siekkinen, A. Warsen, Z. Li, H. Zhang, Y. Xia and X. Li, *Nano Lett.* **7**, 1318 (2007).
22. C. H. Su, H. S. Sheu, C. Y. Lin, C. C. Huang, Y. W. Lo, Y. C. Pu, J. C. Weng, D. B. Shieh, J. H. Chen and C. S. Yeh, *J. Am. Chem. Soc.* **129**, 2139 (2007).
23. N. Tian, Z. Zhou, S. Sun, Y. Ding and Z. L. Wang, *Science* **316**, 732 (2007).
24. C. Wang, H. Daimon, Y. Lee, J. Kim and S. Sun, *J. Am. Chem. Soc.* **129**, 6974 (2007).
25. L. E. Greene, M. Law, B. D. Yuhas and P. Yang, *J. Phys. Chem. C* **111**, 18451 (2007).
26. W. U. Huynh, J. J. Dittmer and A. P. Alivisatos, *Science* **295**, 2425 (2002).
27. Y. Cui, Z. Zhong, D. Wang, W. U. Wang and C. M. Lieber, *Nano Lett.* **3**, 149 (2003).
28. Y. Huang, X. Duan, Y. Cui, L. J. Lauhon, K. Kim and C. M. Lieber, *Science* **294**, 1313 (2001).
29. M. S. Gudiksen, L. J. Lauhon, J. Wang, D. C. Smith and C. M. Lieber, *Nature* **415**, 617 (2002).
30. Z. Zhong, F. Qian, D. Wang and C. M. Lieber, *Nano Lett.* **3**, 343 (2003).
31. S. W. Kim, M. Kim, W. Y. Lee and T. Hyeon, *J. Am. Chem. Soc.* **124**, 7642 (2002).
32. B. Sun, E. Marx and N. C. Greenham, *Nano Lett.* **3**, 961 (2003).
33. D. Wang and C. M. Lieber, *Nat. Mater.* **2**, 355 (2003).
34. H. Zeng, W. Cai, P. Liu, X. Xu, H. Zhou, C. Kling-shirn and H. Kalt, *ACS Nano* **2**, 1661 (2008).
35. C. Kuo and M. H. Huang, *J. Am. Chem. Soc.* **130**, 12815 (2008).
36. L. Manna, E. C. Scher and A. P. Alivisatos, *J. Am. Chem. Soc.* **122**, 12700 (2000).
37. Y. W. Jun, S. M. Lee, N. J. Kang and J. Cheon, *J. Am. Chem. Soc.* **123**, 5150 (2001).
38. S. Chen, Z. L. Wang, J. Ballato, S. H. Foulger and D. L. Carroll, *J. Am. Chem. Soc.* **125**, 16186 (2003).
39. A. Agrawal, T. Sathe and S. Nie, *J. Agric. Food Chem.* **55**, 3778 (2007).
40. J. Kim, J. E. Lee, J. Lee, J. H. Yu, B. C. Kim, K. An, Y. Hwang, C.-H. Shin, J.-G. Park, J. Kim and T. Hyeon, *J. Am. Chem. Soc.* **128**, 688 (2006).
41. T. R. Sathe, A. Agrawal and S. Nie, *Anal. Chem.* **78**, 5627 (2006).
42. D. K. Yi, S. T. Selvan, S. S. Lee, G. C. Papaefthymiou, D. Kundaliya and J. Y. Ying, *J. Am. Chem. Soc.* **127**, 4990 (2005).
43. J. Kim, S. Park, J. E. Lee, S. M. Jin, J. H. Lee, I. S. Lee, I. Yang, J.-S. Kim, S. K. Kim, M.-H. Cho and T. Hyeon, *Angew. Chem. Int. Ed.* **45**, 7754 (2006).

44. J. Kim, J. E. Lee, J. Lee, Y. Jang, S.-W. Kim, K. An, J. H. Yu and T. Hyeon, *Angew. Chem. Int. Ed.* **45**, 4789 (2006).
45. S. I. Stoeva, F. Huo, J.-S. Lee and C. A. Mirkin, *J. Am. Chem. Soc.* **127**, 15362 (2005).
46. B. O. Dabbousi, J. Rodriguez-Viejo, F. V. Mikulec, J. R. Heine, H. Mattoussi, R. Ober, K. F. Jensen and M. G. Bawendi, *J. Phys. Chem. B* **101**, 9463 (1997).
47. M. A. Hines and P. Guyot-Sionnest, *J. Phys. Chem.* **100**, 468 (1996).
48. X. Peng, M. C. Schlamp, A. V. Kadavanich and A. P. Alivisatos, *J. Am. Chem. Soc.* **127**, 7019 (1997).
49. E. Prodan, C. Radloff, N. J. Halas and P. Nordlander, *Science* **302**, 419 (2003).
50. F. Caruso, R. A. Caruso and H. Möhwald, *Science* **282**, 1111 (1998).
51. P. Jiang, J. F. Bertone and V. L. Colvin, *Science* **291**, 453 (2001).
52. L. Lu, R. Capek, A. Kornowski, N. Gaponik and A. Eychmüller, *Angew. Chem. Int. Ed.* **117**, 6151 (2005).
53. C. S. Peyratout and L. Dahne, *Angew. Chem. Int. Ed.* **43**, 3762 (2004).
54. X. Song and L. Gao, *J. Phys. Chem. C* **112**, 15299 (2008).
55. J. Bang and K. S. Suslick, *J. Am. Chem. Soc.* **129**, 2242 (2007).
56. C. Huang, T. Liu, C. Su, Y. Lo, J. Chen and C. Yeh, *Chem. Mater.* **20**, 3840 (2008).
57. H. Qian, G. Lin, Y. Zhang, P. Gunawan and R. Xu, *Nanotechnology* **18**, 355602 (2007).
58. N. A. Dhas and K. S. Suslick, *J. Am. Chem. Soc.* **127**, 2368 (2005).
59. J. Chen, J. M. McLellan, A. Siekkinen, Y. Xiong, Z. Li and Y. Xia, *J. Am. Chem. Soc.* **128**, 14776 (2006).
60. J. Chen, B. Wiley, J. McLellan, Y. Xiong, Z. Li and Y. Xia, *Nano Lett.* **5**, 2058 (2005).
61. Y. Sun and Y. Xia, *Nano Lett.* **3**, 1569 (2003).
62. Y. Vasquez, A. K. Sra and R. E. Schaak, *J. Am. Chem. Soc.* **127**, 12504 (2005).
63. X. Lu, H. Tuan, J. Chen, Z. Li, B. A. Korgel and Y. Xia, *J. Am. Chem. Soc.* **129**, 1733 (2007).
64. P. Selvakannan and M. Sastry, *Chem. Commun.*, 1684 (2005).
65. X. Lu, L. Au, J. McLellan, Z. Li, M. Marquez and Y. Xia, *Nano Lett.* **7**, 1764 (2007).
66. Y. D. Yin, R. M. Rioux, C. K. Erdonmez, S. Hughes, G. A. Somorjai and A. P. Alivisatos, *Science* **304**, 711 (2004).
67. X. Liang, X. Wang, Y. Zhuang, B. Xu, S. Kuang and Y. Li, *J. Am. Chem. Soc.* **130**, 2736 (2008).
68. H. Cao, X. Qian, C. Wang, X. Ma, J. Yin and Z. Zhu, *J. Am. Chem. Soc.* **127**, 16024 (2005).
69. R. K. Chiang and R. T. Chiang, *Inorg. Chem.* **46**, 369 (2007).
70. Y. Xiong, B. Wiley, J. Chen, Z. Li, Y. Yin and Y. Xia, *Angew. Chem. Int. Ed.* **44**, 7913 (2005).
71. Y. Song, R. M. Garcia, R. M. Dorin, H. Wang, Y. Qiu and J. A. Shelnutt, *Angew. Chem. Int. Ed.* **45**, 8126 (2006).
72. S. Cao, Y. Zhu, M. Ma, L. Li and L. Zhang, *J. Phys. Chem. C* **112**, 1851 (2008).
73. L. Li, Y. Chu, Y. Liu and L. Dong, *J. Phys. Chem. C* **111**, 2123 (2007).
74. H. Chen, J. He, C. Zhang and H. He, *J. Phys. Chem. C* **111**, 18033 (2007).
75. Y. Cong, G. Wang, M. Xiong, Y. Huang, Z. Hong, D. Wang, J. Li and L. Li, *Langmuir* **24**, 6624 (2008).
76. J. Ding and G. Liu, *J. Phys. Chem. B* **102**, 6107 (1998).
77. J. Chen, B. Wiley, Z. Li, D. Campbell, F. Saeki, H. Cang, L. Au, J. Lee, X. Li and Y. Xia, *Adv. Mater.* **17**, 2255 (2005).
78. G. Mie, *Ann. Phys.* **25**, 337 (1908).
79. H. Chen, R. Liu, M. Lo, S. Chang, L. Tsai and Y. Peng, J. Lee, *J. Phys. Chem. C* **112**, 7522 (2008).
80. J. Yang, J. Y. Lee, H. P. Too and S. Valiyaveetil, *J. Phys. Chem. B* **110**, 125 (2006).
81. J. Chen, F. Saeki, B. J. Wiley, H. Cang, M. J. Cobb, Z. Li, L. Au, H. Zhang, M. B. Kimmey, X. Li and Y. Xia, *Nano Lett.* **5**, 473 (2005).
82. X. Yang, S. E. Skrabalak, Z. Li, Y. Xia and L. V. Wang, *Nano Lett.* **7**, 3798 (2007).
83. S. Shukla, A. Priscilla, M. Banerjee, R. R. Bhonde, J. Ghatak, P. V. Satyam and M. Sastry, *Chem. Mater.* **17**, 5000 (2005).
84. Y. Cai, H. Pan, X. Xu, Q. Hu, L. Li and R. Tang, *Chem. Mater.* **19**, 3081 (2007).
85. J. Chen, H. Ding, J. Wang and L. Shao, *Biomaterials* **25**, 723 (2004).
86. Y. Hu, Y. Ding, D. Ding, M. Sun, L. Zhang, X. Jiang and C. Yang, *Biomacromolecules* **8**, 1069 (2007).
87. L. R. Hirsch, R. J. Stafford, J. A. Bankson, S. R. Sershen, B. Rivera, R. E. Price, J. D. Hazle, N. J. Halas and J. L. West, *Proc. Natl. Acad. Sci. USA* **23**, 13549 (2003).
88. X. Huang, I. H. El-Sayed, W. Qian and M. A. El-Sayed, *J. Am. Chem. Soc.* **128**, 2115 (2006).
89. L. Au, D. Zheng, F. Zhou, Z. Li, X. Li and Y. Xia, *ACS Nano* **2**, 1645 (2008).
90. G. Chen, D. Xia, Z. Nie, Z. Wang, L. Wang, L. Zhang and J. Zhang, *Chem. Mater.* **19**, 1840 (2007).
91. T. Harada, S. Ikeda, Y. H. Ng, T. Sakata, H. Mori, T. Torimoto and M. Matsumura, *Adv. Funct. Mater.* **18**, 2190 (2008).

92. S. Ikeda, Y. Ikoma, H. Kobayashi, T. Harada, T. Torimoto, B. Ohtanic and M. Matsumura, *Chem. Commun.*, 3753 (2007).
93. Y. H. Ng, S. Ikeda, T. Harada, S. Higashida, T. Sakata, H. Mori and M. Matsumura, *Adv. Mater.* **19**, 597 (2007).
94. M. Chen, Y. Xie, J. Lu, Y. Xiong, S. Zhang, Y. Qian and X. Liu, *J. Mater. Chem.* **12**, 748 (2002).
95. Y. Cheng, Y. Wang, D. Chen and F. Bao, *J. Phys. Chem. B* **109**, 794 (2005).
96. J. W. Grebinski, K. L. Hull, J. Zhang, T. H. Kosel and M. Kuno, *Chem. Mater.* **16**, 5260 (2004).
97. E. Hao, R. C. Bailey, G. C. Schatz, J. T. Hupp and S. Li, *Nano Lett.* **4**, 327 (2004).
98. T. Herricks, J. Chen and Y. Xia, *Nano Lett.* **4**, 2367 (2004).
99. K. L. Hull, J. W. Grebinski, T. H. Kosel and M. Kuno, *Chem. Mater.* **17**, 4416 (2005).
100. J. Joo, H. B. Na, T. Yu, J. H. Yu, Y. W. Kim, F. Wu, J. Z. Zhang and T. Hyeon, *J. Am. Chem. Soc.* **125**, 11100 (2003).
101. M. Kuno, O. Ahmad, V. Protasenko, D. Bacinello and T. H. Kosel, *Chem. Mater.* **18**, 5722 (2006).
102. S. Lee, Y. Jun, S. Cho and J. Cheon, *J. Am. Chem. Soc.* **124**, 11244 (2002).
103. X. Lou, C. Yuan and L. A. Archer, *Chem. Mater.* **18**, 3921 (2006).
104. X. Peng, *Adv. Mater.* **15**, 459 (2003).
105. Z. A. Peng and X. Peng, *J. Am. Chem. Soc.* **124**, 3343 (2002).
106. X. Teng and H. Yang, *Nano Lett.* **5**, 885 (2005).
107. Y. Yin and A. P. Alivisatos, *Nature* **437**, 664 (2005).
108. K. Yong, Y. Sahoo, K. R. Choudhury, M. T. Swihart, J. R. Minter and P. N. Prasad, *Nano Lett.* **6**, 709 (2006).
109. H. Zhang, J. Ding and G. Chow, *Langmuir* **24**, 375 (2008).
110. J. D. Hoefelmeyer, K. Niesz, G. A. Somorjai and T. D. Tilley, *Nano Lett.* **5**, 435 (2005).
111. Y. Jun, M. F. Casula, J. Sim, S. Y. Kim, J. Cheon and A. P. Alivisatos, *J. Am. Chem. Soc.* **125**, 15981 (2003).
112. X. Lou and H. Zeng, *J. Am. Chem. Soc.* **125**, 2697 (2003).
113. S. Firth and P. A. Warburton, *Appl. Phys. Lett.* **89**, 072104 (2006).
114. Y. Zhou, Y. Li, H. Zhon, J. Hou, Y. Ding, C. Yang and Y. Li, *Nanotechnology* **17**, 4041 (2006).
115. A. B. Djurisic, W. M. Kwok, Y. H. Leung, W. K. Chan, D. L. Phillips, M. S. Lin and S. Gwo, *Nanotechnology* **17**, 244 (2006).
116. M. C. Newton, S. Firth, T. Matsuura and P. A. Warburton, *J. Phys. Conf. Ser.* **26**, 251 (2006).
117. J.-S. Choi, Y.-W. Jun, S.-I. Yeon, H. C. Kim, J.-S. Shin and J. Cheon, *J. Am. Chem. Soc.* **128**, 15982 (2006).
118. J. Jiang, H. Gu, H. Shao, E. Devlin, G. C. Papaefthymiou and J. Y. Ying, *Adv. Mater.* **20**, 1 (2008).
119. W. Shi, H. Zeng, Y. Sahoo, T. Y. Ohulchanskyy, Y. Ding, Z. L. Wang, M. Swihart and P. N. Prasad, *Nano Lett.* **6**, 875 (2006).
120. Y. Wei, R. Klajn, A. O. Pinchuk and B. A. Grzybowski, *Small* **4**, 1635 (2008).
121. C. Xu, J. Xie, D. Ho, C. Wang, N. Kohler, E. G. Walsh, J. R. Morgan, Y. E. Chin and S. Sun, *Angew. Chem. Int. Ed.* **47**, 173 (2008).
122. H. Yu, M. Chen, P. M. Rice, S. X. Wang, R. L. White and S. Sun, *Nano Lett.* **5**, 379 (2005).
123. H. Gu, Z. Yang, J. Gao, C. K. Chang and B. Xu, *J. Am. Chem. Soc.* **127**, 34 (2005).
124. Y. Li, Q. Zhang, A. V. Nurmikko and S. Sun, *Nano Lett.* **5**, 1689 (2005).
125. J. Gao, B. Zhang, Y. Gao, Y. Pan, X. Zhang and B. Xu, *J. Am. Chem. Soc.* **129**, 11928 (2007).
126. S. T. Selvan, P. K. Patra, C. Y. Ang and J. Y. Ying, *Angew. Chem. Int. Ed.* **46**, 2448 (2007).
127. T. Hyeon, *Chem. Commun.*, 927 (2002).
128. S.-H. Choi, H. B. Na, Y. I. Park, K. An, S. G. Kwon, Y. Jang, M.-H. Park, J. Moon, J. S. Son, I. C. Song, W. K. Moon and T. Hyeon, *J. Am. Chem. Soc.* **130**, 15573 (2008).
129. J. Gao, W. Zhang, P. Huang, B. Zhang, X. Zhang and B. Xu, *J. Am. Chem. Soc.* **130**, 3710 (2008).
130. H. Gu, R. Zheng, X. Zhang and B. Xu, *J. Am. Chem. Soc.* **126**, 5664 (2004).
131. M. Zanella, A. Falqui, S. Kudera, L. Manna, M. F. Casula and W. J. Parak, *J. Mater. Chem.* **18**, 4311 (2008).
132. K.-W. Kwon and M. Shim, *J. Am. Chem. Soc.* **127**, 10269 (2005).
133. A. Figuerola, A. Fiore, R. D. Corato, A. Falqui, C. Giannini, E. Micotti, A. Lascialfari, M. Corti, R. Cingolani, T. Pellegrino, P. D. Cozzoli and L. Manna, *J. Am. Chem. Soc.* **130**, 1477 (2008).
134. J. Yang, L. Levina, E. H. Sargent and S. O. Kelley, *J. Mater. Chem.* **16**, 4025 (2006).
135. X. Wang, X. Kong, Y. Yu and H. Zhang, *J. Phys. Chem. C* **111**, 3836 (2007).
136. D. Gerion, N. Zaitseva, C. Saw, M. F. Casula, S. Fakra, T. V. Buuren and G. Galli, *Nano Lett.* **4**, 597 (2004).
137. J. M. D. Coey, *Phys. Rev. Lett.* **27**, 1140 (1971).
138. F. Bodker, S. Mørup and S. Linderroth, *Phys. Rev. Lett.* **72**, 282 (1994).
139. G. C. Papaefthymiou, *Mater. Res. Soc. Symp. Proc.* **635**, C2.4.1 (2001).
140. M. R. Cornell and U. Schwertmann, *The Iron Oxide* (VCH, New York, 1996), p. 117.

141. H. Zeng, J. Li, Z. L. Wang, J. P. Liu and S. Sun, *Nano Lett.* **4**, 187 (2004).
142. I. S. Lee, N. Lee, J. Park, B. H. Kim, Y.-W. Yi, T. Kim, T. K. Kim, I. H. Lee, S. R. Paik and T. Hyeon, *J. Am. Chem. Soc.* **128**, 10658 (2006).
143. K. Somaskandan, T. Veres, M. Niewczasc and B. Simard, *New J. Chem.* **32**, 201 (2008).
144. S. Peng, C. Wang, J. Xie and S. Sun, *J. Am. Chem. Soc.* **128**, 10676 (2006).
145. J. Zhang, M. Post, T. Veres, Z. J. Jakubek, J. Guan, D. Wang, F. Normandin, Y. Deslandes and B. Simard, *J. Phys. Chem. B* **110**, 7122 (2006).
146. H.-Y. Park, M. J. Schadt, L. Wang, I.-I. S. Lim, P. N. Njoki, S. H. Kim, M.-Y. Jang, J. Luo and C.-J. Zhong, *Langmuir* **23**, 9050 (2007).
147. Z. Xu, Y. Hou and S. Sun, *J. Am. Chem. Soc.* **129**, 8698 (2007).
148. Y. Bao, H. Calderon and K. M. Krishnan, *J. Phys. Chem. C* **111**, 1941 (2007).
149. W.-R. Lee, M. G. Kim, J.-R. Choi, J.-I. Park, S. J. Ko, S. J. Oh and J. Cheon, *J. Am. Chem. Soc.* **127**, 16090 (2005).
150. H. P. Liang, Y. G. Guo, H. L. Zhang, J. S. Hu, L. J. Wan and C. L. Bai, *Chem. Commun.*, 1496 (2004).
151. H. P. W. Liang, L. J. Wan, C. L. Bai and L. Jiang, *J. Phys. Chem. B* **109**, 7795 (2005).
152. A. D. Schwartzberg, T. Y. Olson, C. E. Talley and J. Z. Zhang, *J. Phys. Chem. B* **110**, 19935 (2006).
153. J. Gao, G. Liang, J. S. Cheung, Y. Pan, Y. Kuang, F. Zhao, B. Zhang, X. Zhang, E. X. Wu and B. Xu, *J. Am. Chem. Soc.* **130**, 11828 (2008).
154. J. Gao, G. Liang, B. Zhang, Y. Kuang, X. Zhang and B. Xu, *J. Am. Chem. Soc.* **129**, 1428 (2007).
155. E. V. Shevchenko, M. I. Bodnachuck, M. V. Kovalenko, D. V. Talapin, R. K. Smith, S. Aloni, W. Heiss and A. P. Alivisatos, *Adv. Mater.* **20**, 4323 (2008).
156. M. Liu and P. Guyot-Sionnest, *J. Phys. Chem. B* **108**, 5882 (2004).
157. P. M. Takahara, C. A. Frederick and S. J. Lippard, *J. Am. Chem. Soc.* **118**, 12309 (1996).
158. P. M. Takahara, A. C. Rosenzweig, C. A. Frederick and S. J. Lippard, *Nature* **377**, 649 (1995).
159. D. Yang, S. S. van Boom, J. Reedijk, J. H. van Boom and A. H. Wang, *Biochemistry* **34**, 12912 (1995).